ANNUAL REPORT

to

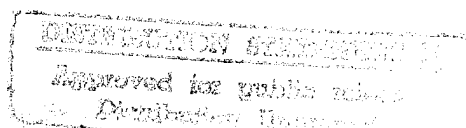## OFFICE OF NAVAL RESEARCH

Contract USN 00014-94-I-0086

January 1996

PREDICTION OF HYDROGEN ENTRY AND PERMEATION IN METALS AND ALLOYS

H. W. Pickering
Department of Materials Science and Engineering
The Pennsylvania State University
University Park, PA 16802

PENNSTATE

College of Earth and Mineral Sciences

DISCLAIMER NOTICE

THIS DOCUMENT IS BEST
QUALITY AVAILABLE. THE
COPY FURNISHED TO DTIC
CONTAINED A SIGNIFICANT
NUMBER OF PAGES WHICH DO
NOT REPRODUCE LEGIBLY.

ANNUAL REPORT

to

OFFICE OF NAVAL RESEARCH

Contract USN 00014-94-I-0086

January 1996

PREDICTION OF HYDROGEN ENTRY AND
PERMEATION IN METALS AND ALLOYS

H. W. Pickering
Department of Materials Science and Engineering
The Pennsylvania State University
University Park, PA   16802

REPORT DOCUMENTATION PAGE

1. AGENCY USE ONLY (Leave blank)	2. REPORT DATE	3. REPORT TYPE AND DATES COVERED
	January 1996	Annual 10/1/94 to 9/30/95

4. TITLE AND SUBTITLE

Prediction of Hydrogen Entry and Permeation in Metals and Alloys

5. FUNDING NUMBERS

N00014-94-I-0086

6. AUTHOR(S)

Howard W. Pickering

7. PERFORMING ORGANIZATION NAME(S) AND ADDRESS(ES)

The Pennsylvania State University
Department of Materials Science and Engineering
326 Steidle Building
University Park, PA 16802

8. PERFORMING ORGANIZATION REPORT NUMBER

9. SPONSORING/MONITORING AGENCY NAME(S) AND ADDRESS(ES)

Scientific Officer
Materials Division Code: 1131M
Office of Naval Research
Arlington, VA 22217-5000
ATTN: A. John Sedriks

10. SPONSORING/MONITORING AGENCY REPORT NUMBER

11. SUPPLEMENTARY NOTES

12a. DISTRIBUTION/AVAILABILITY STATEMENT

Approved for public release; distribution is unlimited.

12b. DISTRIBUTION CODE

13. ABSTRACT (Maximum 200 words)

The ongoing objectives of this research project are to understand the mechanism of hydrogen entry into metals and to search for and evaluate various remedial measures to control this process and the subsequent hydrogen embrittlement. Several parallel approaches are pursued to achieve these objectives. During the last year, significant progress has been achieved on several tasks. A brief description is given below on each of these following tasks: (1) Effect of chloride ions on the evolution and absorption of hydrogen in iron. (2) Effect of benzotriazole (BTA) on the permeability of electrolytic hydrogen through iron. (3) Underpotential deposition and absorption of hydrogen (UPD). (4) Distributions of cathodic and anodic reaction sites during environmentally assisted cracking. (5) Hydrogen evolution and absorption within grain boundary grooves in sensitized stainless steels under anodic protection. (6) Shape evolution of pits and crevices and its role in hydrogen absorption.

14. SUBJECT TERMS KEY WORDS: hydrogen absorption, hydrogen embrittlement, chloride ions, benzotriazole, underpotential deposition, environmental cracking, sensitized stainless steel, anodic protection, pits and crevices, IR drop.

15. NUMBER OF PAGES

16. PRICE CODE

| 17. SECURITY CLASSIFICATION OF REPORT	18. SECURITY CLASSIFICATION OF THIS PAGE	19. SECURITY CLASSIFICATION OF ABSTRACT	20. LIMITATION OF ABSTRACT

TABLE OF CONTENTS

PROJECT SUMMARY

The ongoing objectives of this research project are to understand the mechanism of hydrogen entry into metals and to search for and evaluate various remedial measures to control this process and the subsequent hydrogen embrittlement of steels and other alloys. Several parallel approaches are being pursued to achieve these objectives. During the last year, significant progress has been achieved on several tasks. A brief description is given below on each of these tasks.

1.   **Effect of chloride ions on the evolution and absorption of hydrogen in iron.** The initial step of the hydrogen evolution reaction (HER) in an acid medium is given by:

$$H_3O^+ + e^- \rightarrow H_{ads} + H_2O \tag{1}$$
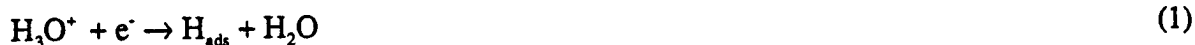
where H_{ads} refers to a hydrogen atom adsorbed on the metal surface. This H_{ads} is involved in the absorption of hydrogen within the metal lattice, i.e.,

$$H_{ads} \text{ (surface)} \rightarrow H_{abs} \text{ (lattice)} \tag{2}$$

We have shown that chloride ions reduce the overpotential for the HER on an iron surface in both acid and alkaline solutions at 23°C, and in turn reduce the hydrogen coverage and permeation of hydrogen. The effects on permeation are more pronounced in alkaline than in acid solutions. Permeation transients at constant electrode potential of the charging surface and subsequent surface analyses of the uppermost atom layers of the hydrogen charged iron surface indicate (1) either a reversible or low coverage with Cl ions, (ii) a low hydrogen coverage which is not influenced significantly by Cl ion concentration at low overpotentials, and (iii) a marked effect of Cl ions on reducing the hydrogen coverage of the surface and the permeability in alkaline solutions at high cathodic polarization. This work has been submitted for publication and is the first paper in the Appendices of this report.

2.   **Effect of benzotriazole (BTA) on the permeability of electrolytic hydrogen through iron.** BTA is a well known inhibitor for Cu and Cu-base alloys. We have obtained some experimental results which show a significant effect of BTA on the permeability of

electrolytic hydrogen through iron membranes and on their polarization behavior. The extent of this effect of BTA was found to be dependent on the level of polarization. Fig. 1 illustrates some of these results. The results are now being completed before they can be analyzed to reveal the mechanism of reaction of BTA.

3. **Underpotential deposition and absorption of hydrogen (UPD):** The question of underpotential deposition of hydrogen is of particular concern to the problem of hydrogen embrittlement. For the case of hydrogen, underpotential deposition refers to hydrogen evolution (and hence absorption within the metal) at potentials more noble than the equilibrium potential of the hydrogen reaction by several tens of millivolts. We have obtained some preliminary results on the UPD of hydrogen on Pd where it was found that hydrogen enters and diffuses through Pd while its surface is controlled at a more noble potential than the equilibrium potential of the hydrogen reaction. These measurements will be continued, and the results analyzed, so that we can obtain a satisfactory mechanism for the process, before testing the same phenomenon on iron.

4. **Distributions of cathodic and anodic reaction sites during environmentally assisted cracking.** We have recently shown that the presence of significant IR potential drop within cracks leads to nonuniform distribution of both the cathodic and anodic reaction sites on the flanks of these cracks. For the case of cathodic protection in an acid medium, it has been found that a characteristic depth Z controls the above distributions:

$$Z = \left[\frac{FDC^o a}{i_o} \exp\left(\frac{\beta\eta(0)}{b} \right) \right]^{1/2} \text{cm} \tag{3}$$

where C^o and D are the concentration and diffusivity of H_3O^+, a is the crack width and i_o, β and $\eta(0)$ are the exchange current density, transfer coefficient and overpotential of the hydrogen evolution reaction. The analysis of the problem yielded quantitative relations which can be used to evaluate the efficiency of cathodic protection on surfaces with recesses or cracks. This work was recently published: B. G. Ateya and H. W. Pickering, Corros. Sci., 37 (9), 1443-1453 (1995), and is the second paper in the Appendices of this report.

5. **Hydrogen evolution and absorption within grain boundary grooves in sensitized stainless steels under anodic protection.** Progress in this area includes experimental evidence for the electrolytic generation of hydrogen within the grain boundary grooves of sensitized 430 stainless steel membranes while the outer surfaces are anodically polarized with respect to the hydrogen evolution reaction. We have also analyzed the kinetics of

intergranular corrosion of the Cr-depleted zones in the steel and proved a synergistic effect of Cr-depletion and ohmic potential drop on the susceptibility to intergranular corrosion and hydrogen embrittlement of the steel. The grooves form at the steel surface with openings characteristic of the width of the Cr-depleted zone (~< 0.2 μm). They deepen and branch out beneath the surface and attack the bulk alloy of normal Cr-content within the membrane. The electrode potentials at such locations allow for hydrogen evolution, which is prohibited at the steel surfaces. A Devanathan-Stachurski cell was used to detect the permeation of this hydrogen through the steel. The crevices which form around the Cr-depleted zone propagate until they eventually perforate the membrane. This progress was made possible by the developments of a novel experimental technique to detect this stage of the corrosion process. Part of this work was recently published: A. Sehgal, B. G. Ateya and H. W. Pickering, J. Electrochem. Soc., 142 (10), L198 - 1200 (1995), and is the third paper in the Appendices of this report.

6. **Shape evolution of pits and crevices and its role in stimulating hydrogen absorption.** The question of shape evolution of pits and crevices is of fundamental importance in localized corrosion and in hydrogen embrittlement. This shape evolution follows the current distribution on the sides of the cavity, which is determined by the potential distribution within the electrolyte phase inside the cavity. The latter, in turn, is determined primarily by the resistivity of the electrolyte filling the cavity, which may include gas bubbles and/or solid corrosion products. Within such constricted cavities, we have earlier shown that electrolytic hydrogen can be generated, which eventually can lead to embrittlement. The question of shape evolution poses a challenge on the levels of physical and mathematical modeling and of experiment measurements.

During this year, we succeeded in monitoring the potential distribution and shape evolution of cyclindrical crevices (artificial pits) in nickel immersed in an acid medium. The results were interpreted in the light of a mathematical model which was published earlier. The model was found to accurately predict the aspect ratio which causes proton discharge and hydrogen absorption from within the cavity. Only crevices with depths greater than the critical depth predicted by the above mentioned model (which is based on fundamental principles and requires no adjustable parameters) actively corroded. The upside down orientation led to convective mixing as the corrosion products flowed downward out of the crevices. This maintained the low pH0 condition and large size of the active peak, thereby stabilizing the crevice corrosion process in accordance with the magnitude of the IR drop in the crevice. This work was recently published: M. Wang, H. W. Pickering and Y. Xu. J. Electrochem. Soc. 142 (9), 2986 - 2995 (1995), and is the fourth paper in the Appendices of this report. (Fig. 5 illustrates the various stages of the shape evolution).

These experiments have also given new insight into the role of pH and the dynamics of interaction between the IR potential drop and other composition changes (e.g., metal ion concentration) during the activation and propagation of crevices. The potential distribution is emerging more and more as the dominant factor in the activation and propagation of crevices. The major importance of localized acidification is shown to have its effect through its role in increasing the size of the active peak. The IR potential drop is necessary to shift the electrode potential, from the passive values at the crevices external surface, to within the active peak (which has been expanded by acidification and/or Cl⁻ accumulation) inside the crevice. The most recent aspects of this work have been submitted for presentation at a symposium on crevice corrosion at Corrosion '96, Denver, CO, in March 1996. Another part was submitted for presentation at the Second Arabian Corrosion Conference, organized by Kuwait, October 12-15, 1996.
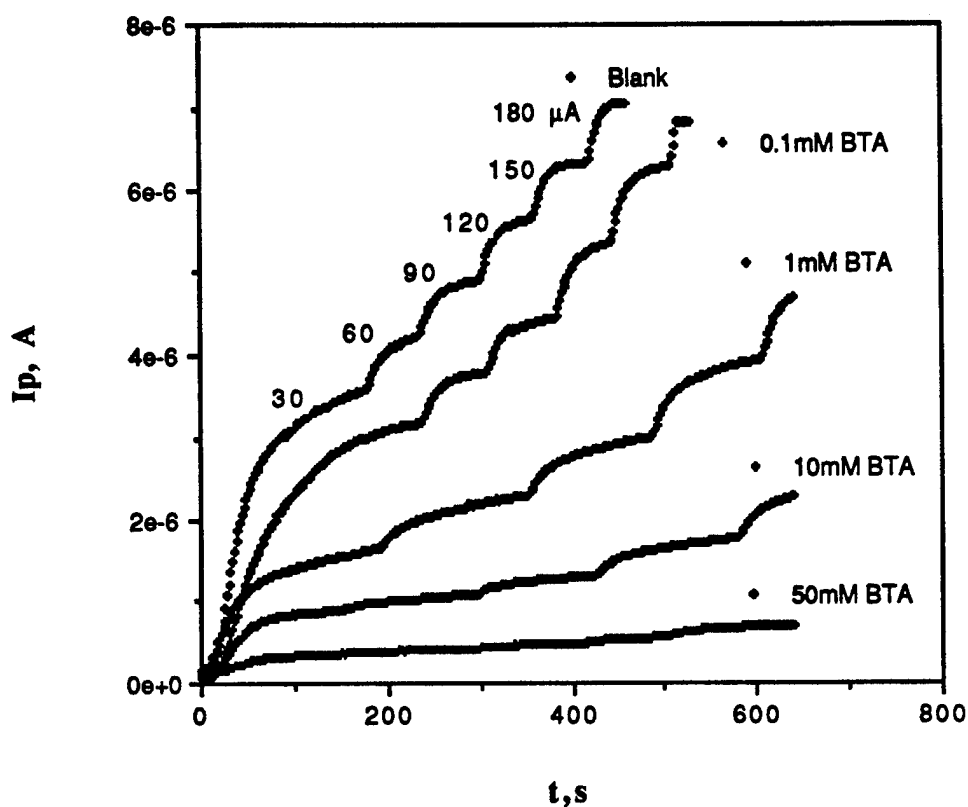
Fig.1 Hydrogen permeation transients obtained at different cathodic currents (30-180 μA), and for various concentrations of BTA in acidic solution of 0.1N H_2SO_4+ 0.9N Na_2SO_4, for an annealed iron membrane of thickness 0.25 mm, which illustrate the strong effect of BTA on inhibiting hydrogen absorption.

PUBLICATIONS ON THE PROJECT

B. G. Ateya and H. W. Pickering, "The Distribution of Anodic and Cathodic Reaction Sites During Environmentally Assisted Cracking", Corros. Sci., 37 (9), 1443-1453 (1995).

A. Sehgal, B. G. Ateya and H. W. Pickering, "Hydrogen Evolution and Absorption Within Grain Boundary Grooves in Sensitized Stainless Steel Under Conditions of Anodic Polarization", J. Electrochem. Soc., 142 (10), L198-L200 (1995).

M. Wang, H. W. Pickering and Y. Xu, "Potential Distribution, Shape Evolution and Modeling of Pit Growth for Ni in Sulfuric Acid", J. Electrochem. Soc., 142 (9), 2986-2995 (1995).

H. W. Pickering, "The Role of Electrode Potential Distribution in Corrosion Processes", J. Materials Sci. & Eng. A, 198, 213-223 (1995).

A. A. Allam, B. G. Ateya and H. W. Pickering, "Effect of Chloride Ions on the Absorption and Permeation of Hydrogen in Iron", submitted to Corrosion Journal.

E. A. Nystrom, H. W. Pickering and A. A. Sagüés, "Current and Potential Distributions Inside Crevices in Rebar Steel and Other Metals", Proc. First Mexican Symposium on Metallic Corrosion, Paper 74, pp. 1-11, L. Maldonado and M. Pech, eds., ISBN 968-36-4811-8, UNAM Facultad de Quimica Press, Mexico D. F., 1995.

A. Sehgal, B. G. Ateya and H. W. Pickering, "Synergistic Effects of Chromium Depletion and Ohmic Potential Drop on the Susceptibility to Intergranular Corrosion and Hydrogen Embrittlement of Sensitized Stainless Steel", submitted to Acta Metallurgica et Materialia.

B. G. Ateya and H. W. Pickering, "The Dynamics of Interaction Between the IR Potential Drop and Composition Changes During the Activation and Propagation of Crevice Corrosion", Proc. Research Symp. on Crevice Corrosion (CORROSION 96, Mar. 25-29, 1996, Denver, CO).

B. G. Ateya and H. W. Pickering, "The Mechanism of Shape Evolution in Localized Corrosion Cells", Extended Abstract for Second Arabian Corrosion Conference, Oct. 12-15, 1996, Kuwait.

EFFECT OF CHLORIDE IONS ON THE ABSORPTION AND PERMEATION OF HYDROGEN IN IRON

by

A. M. Allam[*], B. G. Ateya[**], and H. W. Pickering
Department of Materials Science and Engineering
The Pennsylvania State University
University Park, PA 16802

ABSTRACT

The effect of Cl^{-} ion on the absorption of hydrogen into iron and on the hydrogen evolution reaction (h.e.r.) on an iron surface was studied in acid and alkaline solutions at 23°C using the permeation method of Devanathan and Stachurski. Chloride ions reduced the overpotential for the h.e.r. and, in turn reduced the hydrogen coverage and permeation of hydrogen. The effects on permeation are more pronounced in alkaline than in acid solutions. Permeation transients at constant electrode potential of the charging surface and subsequent surface analyses of the uppermost atom layers of the hydrogen charged iron surface indicate (i) either a reversible or low coverage with Cl^{-} ions, (ii) a low hydrogen coverage which is not influenced significantly by Cl^{-} ion concentration at low overpotentials, and (iii) a marked effect of Cl^{-} ions on reducing the hydrogen coverage of the surface and the permeability in alkaline solutions at high cathodic polarizations.

---

[*] Deceased
[**] Permanent address: Chemistry Department, Faculty of Science, Cairo University, Cairo, Egypt

INTRODUCTION

The effects of chloride ions on pitting, stress-corrosion cracking and general corrosion have been well-documented.[1-7] On the other hand, their effects on the kinetics of the hydrogen evolution reaction (h.e.r.), and hence on hydrogen absorption and permeation through iron, is less certain and there is an evident shortage of published work on this point.[8,9] This is the more surprising since extensive work has been published[10-21] (and more recent references) on the effects of various additives, e.g., CN^-, I^-, naphthalene, and As^{3+} on the hydrogen evolution reaction, and/or on hydrogen permeation. The purpose of this paper is to study simultaneously the effect of Cl^- ions on(i) the absorption of hydrogen by iron during cathodic hydrogen charging, and (ii) the polarization behavior of the hydrogen evolution reaction.

EXPERIMENTAL

The Devanathan and Stachurski method[22] was used to measure the permeability of hydrogen through Ferrovac E iron membranes as a function of the charging current density and the level of the Cl^- ion concentration in the charging solution. It consists of two identical electrolytic cells separated by the iron membrane. One cell (Cell 1) is used to generate the hydrogen charging current and to measure the potential of the charging side of the membrane under various conditions of current, and Cl^- concentration, while the other (Cell 2) is used to measure the hydrogen oxidation current at the exit surface of the iron membrane which is a direct measure of the flux of hydrogen diffusing through the membrane.

The reference electrode in cell 1 was Hg/HgO in the alkaline and Hg/Hg_2SO_4 in the acid solutions. Cell 2 was filled with 0.1N NaOH and a Hg/HgO reference electrode was used in it. Potentials are reported in terms of the standard hydrogen electrode (SHE). The measurements were carried out at $23\pm2°C$.

The Pt counter electrodes in both cells were separated from the respective working electrode compartments by thick, medium porosity, glass frits since Pt is known to dissolve in Cl^- solution[23]. In order to check that dissolved Pt had not entered the working electrode compartment

and had not deposited on the iron surface, this surface was rinsed with distilled water and subsequently analyzed by Auger electron spectroscopy (AES) and by X-ray photoelectron spectroscopy (XPS). No platinum was detected on the surface.

Ferrovac E iron membranes, 0.055 cm thick, were given a final polish with 600 emery paper; degreased in a Soxhlet condenser for about 24 hours using 50/50 benzene-methanol mixture; annealed in evacuated capsules at 1000°C for 2 hours and furnace cooled prior to insertion in the permeation cell.

The exit surface, which was Pd coated, was maintained at 0.10 V (SHE), which is sufficient to oxidize the hydrogen atoms reaching this surface. The permeation current was constant for a wide range of potentials on both sides of this value. The residual current was ~0.2 μA cm^{-2}. The Pd layer, applied by chemical deposition, minimized loss of hydrogen as H_2 gas[10,22,24].

Strict conditions of purity and deareation were maintained throughout the measurements. Distilled water was prepared following the method of Powers[25]. The solutions were pre-electrolyzed overnight using a Pt anode separated by a glass frit from the main electrolyte containing an Fe cathode under an atmosphere of prepurified nitrogen. They were transferred from the pre-electrolysis cell to the working cell under nitrogen. Details of the membrane preparation, cell design, circuitry, electrochemical conditions, proper membrane thickness and edge effect, as well as other experimental conditions, are presented elsewhere[26].

The potential measured at the charging side of the membrane includes an ohmic drop between the tip of the Luggin capillary and the membrane surface, and a liquid junction potential (between dissimilar electrolytes) in addition to the activation and concentration polarizations. The ohmic and concentration polarizations are considered negligible since measurements were confined to low cathodic charging currents. The error introduced by a variation in liquid junction potential and/or activity coefficient of H$^+$ ion with changing ionic strength of the charging electrolyte was evaluated by the following experiment:

Two large area platinized Pt electrodes were brought to a zero current flow condition under a H_2-gas pressure of 1 atm., one in the Cl$^-$-containing and the other in the Cl$^-$-free acid solutions.

The compartments of the two electrodes were connected by a Luggin capillary identical to that used in the measurements. The measured potential difference was -0.2 mV between two blank solutions, 3.2 mV between blank and 0.1N NaCl solutions, and -0.3 mV between blank and 1N NaCl solutions. Since these potential difference are small relative to those which were measured in the experiments and attributed to the effects of Cl^- ions, the combined effects due to liquid junction potential and variations in activity coefficient can be neglected.

All measurements were taken in the following sequence: First the blank, then the 0.1N NaCl and, finally, the 1N NaCl solutions. With each solution, data were obtained for a series of charging currents. Thus, three series were performed consecutively on each membrane. The procedure differed slightly for the acid and alkaline charging solutions. In order to remove the air-formed oxide on the Fe membranes, they were hydrogen charged at either 10 or 2 mA cm^{-2} for 30 minutes in the blank alkaline or acid solutions, respectively. This pretreatment has been frequently recommended[27,28] and was found in this work to give reproducible results of permeation current, i_∞, and electrode potential, E. The resulting Tafel plots, Fig. 1, are in good agreement with those reported in the literature[18,19]. The hydrogen charging current was then decreased in a stepwise manner as steady permeation currents and potentials were obtained ($\gtrsim$ 4 minutes). With the NaOH solutions, the charging current was shut off for up to 2 minutes between transients while the permeation current decayed to a low value, a procedure which was avoided in the H_2SO_4 solutions because of the possibility that the membrane would undergo dissolution.

RESULTS

Figure 1 shows the Tafel plots of the h.e.r. at the charging side of the membrane for both acid and alkaline solutions (blank, 0.1N and 1N Cl^- ions). The overvoltage for hydrogen evolution is less in the chloride-containing solutions. The Tafel slope, $\frac{\partial \eta}{\partial \ln i_c}$, is 120 ± 2 mV in the acid solution regardless of the presence or level of Cl^- ions in the electrolyte,, and 115 ± 4 mV and 133 ± 4 mV in the blank and Cl^- containing alkaline solutions, respectively. These values of Tafel slopes are in the range of those reported for iron by other workers in a variety of electrolytes[18,19].

However, they indicate that the Cl ions have a moderate effect on the structure and potential profile within the double layer only in an alkaline solution and no such effects are observed in acid solution.

Figure 2 shows the steady-state permeation current, i_∞ as a function of charging current and chloride concentration. For both alkaline and acid solutions the permeation of hydrogen decreases with increasing concentration of Cl$^-$ ion for the same value of charging current. This effect of chloride ion is reproducible, though varying in magnitude from specimen to specimen. Thus, to that extent the Cl$^-$ ion enhances the hydrogen evolution reaction and retards the absorption reaction.

Figure 3 shows that at constant overvoltage the effect of Cl$^-$ ion on hydrogen permeation is negligible except in the alkaline solutions at the higher potentials where increasing chloride concentration significantly decreases permeation. Thus, especially at low overvoltages in both solutions, the relation between overvoltage and permeation is not disturbed by the presence of Cl$^-$ ion in the electrolyte or presumably on the surface.

The surfaces of the charged membranes were analyzed after thorough rinsing in doubly distilled water using AES and XPS, with both giving similar results. The AES scans show the following: (i) absence of platinum contamination on the surface, and (ii) a chloride level on the surface which is very low and independent of the chloride concentration in the charging solution, and decreases with ion bombardment. There were no Cl$^-$ peaks greater than the contamination level indicated for the blank (1N H$_2$SO$_4$) solution. A difficulty, however, exists in these forms of surface analyses in that chloride may be removed from the surface by the beam itself[29,30]. To check for this, the beam was moved from position to position on the surface with Cl recorded early in the scan (usually 10 s); the level of Cl$^-$ remained essentially unchanged.

DISCUSSION

The presence of Cl⁻ ions in the electrolyte facilitates the hydrogen evolution reaction in acid as well as in alkaline solution (Fig. 1). The magnitude of the change in the overpotential, η, for hydrogen evolution with increasing Cl⁻ concentration is slightly less than that indicated in Fig. 1 (change of E at constant i_c) since some of the ΔE is due to the change in the potential distribution across the double layer. The latter occurs in view of the variation in ionic concentration and accompanying redistribution of charge in the double layer that accompanies the addition of Cl⁻ ions to the bulk solution. Thus, $\Delta E = \Delta\eta + \Delta\xi$ where $\Delta\xi$ is the change in potential across the diffuse double layer[31]. The latter, in addition to being small compared to ΔE is also not likely to account for the observed change in permeation (Fig. 2), i.e., it would not likely produce a significant change in any of the hydrogen permeation parameters (hydrogen coverage or the rate constants of the adsorption/absorption reaction).

A widely discussed view of the behavior of chloride ions is that they interact strongly with the iron surface. This interaction on iron and other metals has been proposed for open circuit and anodic polarization conditions to be in the form of adsorption[32,33,34] or even the formation of a surface complex[35,36]. An analysis of the effect of Cl⁻ ion on the entry of hydrogen into Fe can begin with a consideration of a model for a coupled discharge-recombination mechanism of hydrogen evolution on iron given by Bockris et al.[10]. These authors arrived at the following limiting relation between the hydrogen charging current, i_c, and the steady state permeation current, i_∞ which holds for $i_p \ll i_c$:

$$i_\infty \cong \frac{FD}{L}\frac{\bar{K}}{\bar{\bar{K}}}\left(\frac{1}{K}\right)^{1/2} i_c^{1/2} \qquad (1a)$$

In the general case one has:[37,38]

$$i_\infty = \frac{FD}{L}\frac{\bar{\vec{K}}}{\bar{K}}\left(\frac{1}{K}\right)^{1/2} i_r^{1/2} \tag{1b}$$

which hold for all values of i_p and i_c,

where F is the Faraday constant, D is the diffusivity of hydrogen in the metal, L is the metal membrane thickness, $\vec{K}$ and $\overleftarrow{K}$ are, respectively, the forward and the backward standard rate constants of the reaction

$$H_{ads}\ (surface) \underset{\overleftarrow{K}}{\overset{\bar{K}}{=}} H_{ab}\ (lattice) \tag{2}$$

K is the standard rate constant and i_r is the recombination current of the H_2 formation step. The overall h.e.r. on iron in acid solution is given by,

$$H_3O^+ + e^- \rightarrow \frac{1}{2}H_2 + H_2O \tag{3}$$

The first step in this reaction is

$$H_3O^+ + e^- \xrightarrow{K_d} H_{ads} + H_2O \tag{4}$$

which is followed by reaction of Hads to form H_2 molecules. At low coverages H_2 is likely to form by the chemical path,

$$2H_{ads} \xrightarrow{K} H_2 \tag{5a}$$

although the electrochemical path,

$$H_{ads} + H_3O^+ + e^- \xrightarrow{\;K\;} H_2 \qquad (5b)$$

is also consistent with the model. There are several assumptions involved in arriving at Eq. (1a), namely (i) that reaction (2) is at equilibrium and transport through the membrane controls the permeation rate; (ii) that the intermediate H_{ads} involved in the absorption step, Eq. (2), is the same one involved in the H_2 formation step, Eq. (5); (iii) a low hydrogen coverage and (iv) a low solubility of hydrogen in the metal. Then, $i_\infty \ll i_c$ where

$$i_c = K\,\theta_H^2 \qquad (6)$$

and

$$i_c = K_d\, a_{H_3O^+}\, (1 - \theta_H - \theta_{Cl})\, \exp\,(-\beta\Delta\phi F/RT) \qquad (7)$$

The coverage quantities θ_H and θ_{Cl} are the fractions of the surface covered with adsorbed hydrogen and chloride, respectively; K_d is the rate constant of reaction (4); $a_{H_3O^+}$ is the activity of the H_3O^+ ion; β is the symmetry factor of the activation barrier for discharge; $\Delta\phi$ is the potential difference across the iron/solution interface; and F, R, and T have their usual meanings.

The straight lines which pass through the origin in Fig. 2 are consistent with the form of Eq. (1a) and hence, the underlying model. It is also clear that the presence of Cl^- ion causes the following: (i) a decrease in i_∞ at the same i_c, and (ii) a decrease in slope. According to Eq. (1a), the slopes of the straight line segments passing through the origin in Fig. 2 are given by

$$slope = \frac{FD}{L}\; \frac{\bar{K}}{\bar{\bar{K}}}\, (\frac{1}{K})^{1/2} \qquad (8)$$

Consequently, a decrease in the value of the slope can be brought about by either an increase in the rate constant of the H_2 formation step, K, corresponding to a decreased θ_H (Eq. (6)), and/or a shift in the equilibrium of reaction (2) to the adsorption side. A decreased overpotential η at constant

charging current i_c, due to Cl^- ion (Fig. 1), is consistent with an increase in either the rate constant of the discharge reaction, K_d, or the activity of the H_3O^+ ion (Eq. (7)) in the case of low total coverages.

The results in Figure 2 are consistent with data reported by various groups [9,39]. In contrast, permeation of hydrogen increases for other halogen ions, I^-, Br^- [10-12,17] and for H_2S [40,41], although H_2S behaves similarly to Cl^- as a promoter of the h.e.r. [41,42].

The same amount of Cl^- was indicated on the surface after charging in either acid or alkaline solutions of different Cl^- ion concentration. This suggests that if chloride ion is adsorbing in proportion to its concentration in solution, it readily desorbs when the potential changes to the open circuit value or when the membrane contacts a less concentrated solution (e.g., rinse water). This is in agreement with the results reported by Smialowska et al[43], who observed that Cl^- ions are rather weakly bonded to the iron surface under either anodic or cathodic polarization conditions. The same may be said for $SO_4^=$ which is present to an even lesser degree according to the surface analysis data. Such a reversible behavior has been previously observed for the adsorption of Cl^- on Pt using a radioactive tracer technique [32] and on iron using ac-impedance[8]. Consequently, strong or preferred adsorption of Cl^- may not be occurring in which case the concentration of Cl^- ion in the double layer becomes the important factor in determining the kinetics of the h.e.r.

From Fig. 3 it is seen that over a broad region of low overpotential, hydrogen permeation is independent of the Cl^- ion concentration. This, in turn, implies that for these overpotentials the coverage of hydrogen is not a function of Cl^- ion concentration, assuming no shift in the equilibrium of reaction (2). These results are consistent with the hypothesis that the chloride coverage is not very high, since then it could increase with an increase in Cl^- concentration in the solution without affecting a low hydrogen coverage. Combining Eqs. (6) and (7), and allowing $1-\theta_H-\theta_{Cl}$ to approach unity corresponding to low coverages by H and Cl^-, Eq. 9 is obtained.[10]

$$\theta_H \cong \left[\frac{AK_d a_{H_3O^+}}{K} \right]^{\frac{1}{2}} \exp(-\beta\eta F / 2RT) \qquad (9)$$

Where the quantities A and $\Delta\phi_e$ are exp $(-\beta\Delta\phi_e F/RT)$ and the potential gradient across the iron/solution interface at equilibrium, respectively. For the i_∞ data in Fig. 3 which show no dependence on Cl$^-$ ion concentration, it follows that the term in brackets in Eq. 9 is also independent of chloride ion concentration. Thus, the rate constants of the discharge, K_d, and H$_2$ formation, K, steps respond to the presence of chlorine ion in a coupled manner, i.e., each (K_d and K) increases equally if the quantity in the brackets is constant. This is consistent with the reported mechanism of the h.e.r. on iron in acid[10,44]. Actually, they increase equally with increasing Cl$^-$ content, assuming no change in the rate constants of the absorption/adsorption step (Eq. 2) so that a constant i_∞ means a constant θ.

At higher overpotentials in Fig. 3 chloride ion does have an effect on hydrogen permeation especially for the alkaline solution, causing a decrease in i_∞. Following the above reasoning the hydrogen coverage may now be high enough (Eq. 9) so that an increase in ϕ_{Cl} (due to an increase of Cl$^-$ ion in the solution) causes a decrease in ϕ_H and a resulting decrease in i_∞. Results of others[45-49] on Pt and Pd surfaces show a similar trend.

The transition potential between the presence and absence of a Cl$^-$ effect for alkaline solutions in Fig. 3 (about -1.0 V SHE) corresponds to the charging current at which the inflection occurs in Fig. 2b. The inflection occurs at a less negative potential the higher the Cl$^-$ concentration. These inflections are similar to those observed by others in the presence and in the absence of various poisons, e.g., CN$^-$, I$^-$, and naphthalene[10-17], which were explained in terms of a change in the mechanism of the h.e.r.[24]. A similar shift to less negative potentials with increasing Cl$^-$ concentration is also seen in the data when compared at the same pH of McCafferty and Hackerman[50].

CONCLUSIONS

Increasing Cl$^-$ ion concentration in 1N H$_2$SO$_4$ causes an increase in the h.e.r. and a decrease in i_∞ for a given i_c but no significant change in the hydrogen permeation rate at constant potential

over a significant potential range (especially in acid solutions). A constant permeation rate at constant potential is indicative of a weak effect of Cl^- ion on hydrogen coverage. A reversible adsorption and low coverage are indicated for the chloride ion.

ACKNOWLEDGMENT

REFERENCES

1. Z. Szklarska - Smialowaka, Pitting Corrosion, NACE, Houston (1986).

2. John R. Scully and Patrick J. Moran, J. Electrochem.Soc., 135, 1337 (1988).

3. J. R.Scully and P. J. Moran, Corrosion, 44, 176 (1988).

4. Yozo Sawaki, Shuji Tada, Tadashi Kawasaki and Shizmo Nomura, Nippon KiKai Gakkai Ronbunshu, A Hen v 52 n 482, pp 2324 - 2330 (1986).

5. I. H. Craig and R. N. Parkins, Br. Corros. J., 19, 3 (1984).

6. Guenter Schmitt and Bernhard Olbertz, Werkstoffe und Korros., 29, 451 (1978).

7. Rokuro Nishimura, Corros. Sci., 34, 1859 (1993).

8. Lj. Vrač ar and D. M. Drazic, J. Electroanal. Chem., 339, 269 (1992).

9. G. V. Khaldeev and T. F. Borisova, Elektrokhim., 24, 618 (1988).

10. J. O'M Bockris, J. McBreen and L. Nanis, J. Electrochem. Soc., 112, 1025 (1965).

11. A. N. Frumkin, Advan. in Electrochem. and Electrochem. Eng., Vol. 3, p. 377, P. Delahay and C. Tobias, Editors, Interscience Publishers, N.Y. (1963).

12. T. P. Radhakrishnan and L. L. Shrier, Electrochem. Acta, 11, 1007 (1966).

13. J. F. Newman and L. L. Shrier, Corrosion Sci., 9, 631 (1969).

14. T. Zakroczmski, A. Szklarska-Smialowska and M. Smialowskil, Werstoffe und Korrosion, 27, 625 (1976).

15. T. Zakroczmski, A. Szklarska-Smialowska and M. Smialowski, Werstoffe und Korrosion, 26, 617 (1975).

16. A. Kawshima, K. Hashimoto and S. Shimodaira, Corrosion, 32, 321 (1976).

17. J. McBreen and M. A. Genshaw, Proceedings of International Conference on Fundamental Aspects of Stress Corrosion Cracking, p. 51, R. W. Staehle, A. J. Forty and O. Van Rooyen, Ed. NACE (1969).

18. M. Enyo in "Comprehensive Treatise of Electro-Chemistry", Vol. 7, p. 241, B. E. Conway, J. O' M. Bockris, E. Yeager, S. U. M. Khan and R. E. White, Ed., Plenum, New York (1983).

19. A. J. Appelby, H. Kita, M. Chemla and G. Bronoël in "Encycolpedia of the Electrochemistry of the Elements", Vol. IX, p. 384, Part A, J. Bard, ed., Dekker, New York (1982).

20. I. A. Ammar, S. Darwish and M. Etman, Electrochim. Acta. 12,485, (1967); I. A. Ammar, S. Darwish and W. Khalil, ibid., 657.

21. R. D. McCright and R. W. Staehle, J. Electrochem. Soc., 121. 609 (1974).

22. M. A. V. Devanathan and Z. Stachurski, Proc. Roy. Soc., A270, 90 (1962); M. A. V. Devanathan, Z. Stachurski and W. Beck, J. Electrochem. Soc. 110, 886 (1963).

23. R. P. Frankenthal and H. W. Pickering, J. Electrochem. Soc., 112, 514 (1965).

24. M. A. V. Devanathan and Z. Stachurski, J. Electrochem. Soc., 111, 619 (1964); W. Beck, J. O'M. Bockris, M. A. Genshaw and P. K. Subramanyan, Metallurgical Transactions 2, 883 (1971).

25. R. W. Powers, Electrochemical Technology, May-June, 163 (1964).

26. S. S. Chatterjee, B. G. Ateya and H. W. Pickering, Met. Trans. 9A, 389 (1978).

27. S. Wack, A. P. Moidownik, and J. Mackowiat, Corr. Sci., 6, 271 (1966).

28. S. Wack, Br. Corros. J., 6, 114 (1971).

29. C. G. Pantano and T. E. Madey, Appl. Surf. Sci., 7, 115 (1981).

30. S. Bouquet, J. Bergner, J. LeHericy and J. P. Langeron, J. Electr. Spec. and Related Phenom., 26, 247 (1982).

31. K. J. Vetter, Electrochemical Kinetics, p. 563, Academic Press, N. Y. (1967).

32. G. Horanyi and G. Inzelt, J. Electroanal. Chem., 86, 215 (1978).

33. T. Murakaura, S. Nagaura and N. Hackerman, Corrosion Science 7, 79 (1967); T. Murakana, T. Kato, S. Nagaura and N. Hackerman, ibid, 8, 483 (1968).

34. R. Gomez, J. M. Feliu and H. D. Abruna, J. Phys. Chem., 98, 5514 (1994).

35. R. T. Foley, Corrosion, 26, 58 (1970).

36. X. C. Jiang, M. Seo and N. Sato, J. Electrochem Soc., 137, 3804 (1990).

37. E. G. Dafft. K. Bohnenkamp, and H. J. Engell, Corros. Sci., 19, 591 (1979).

38. R. N. Iyer, H. W. Pickering and M. Zamanzadeh, J. Electrochem. Soc., 136, 2463 (1989).

39. R. M. Hudson, Corrosion, 20, 245t (1964)

40. I. N. Putilova, S. A. Balezin and V.P. Barannik, Metallic Corrosion Inhibitors, p. 112, Pergamon Press, (1960).

41. I. Takeuchi, M.S. Thesis, The Pennsylvania State University (1980); R. N. Iyer, I. Takeuchi, M. Zamanzadeh and H. W. Pickering, Corrosion, 46, 460 (1990).

42. A. Kawashma, K. Hashimoto and S. Shimodaira, Corrosion, 32, 321 (1976); Z. A. Iofa and F. L. Kam Zashchita Metallov, 10, 300 (1974).

43. Z. Szklarska-Smialowska, H. Viefhaus and M. Janik-Czachor, Corrosion Sci., 16, 649 (1976).

44. N. D. Tomashov and L. P. Vershinina, Electrochemica Acta, 15, 501 (1970).

45. M. W. Breiter, J. Electroanal. Chemi., 90, pp. 425-430 (1978).

46. Zn. Vert, I. A. Mosevich and I. Tverdovshy, Dokl. Akad, Nauk SSSR, 140, 149 (1961).

47. V. S. Vilinskaya, R. H. Burshtein and M. R. Jarasevich, Elektrokhimiya, 6, 1497 (1970).

48. R. H. Burshtein, V. S. Bilinskaya and M. R. Tarasevich, Elektrokhimiya, 6, 1861 (1970).

49. A. Slygin, A. Frumkin and W. Medwedousky, Acta Physicochim. URSS, 4, 911 (1936).

50. E. McCafferty and N. Hackerman, J. Electrochem. Soc., 119, 999 (1972).

FIGURE CAPTIONS

1. Effect of Cl^- ion on the Tafel plots of the hydrogen evolution reaction at the charging side of an iron membrane.

2. Effect of Cl^- ion on the steady-state hydrogen permeation current, i_∞, as a function of the square root of the charging current, i_c. (a) Acid solutions. (b) Alkaline solutions.

3. Effect of Cl^- ion on the relation between the steady-state hydrogen permeation current and electrode potential of the charging surface of the iron membrane.
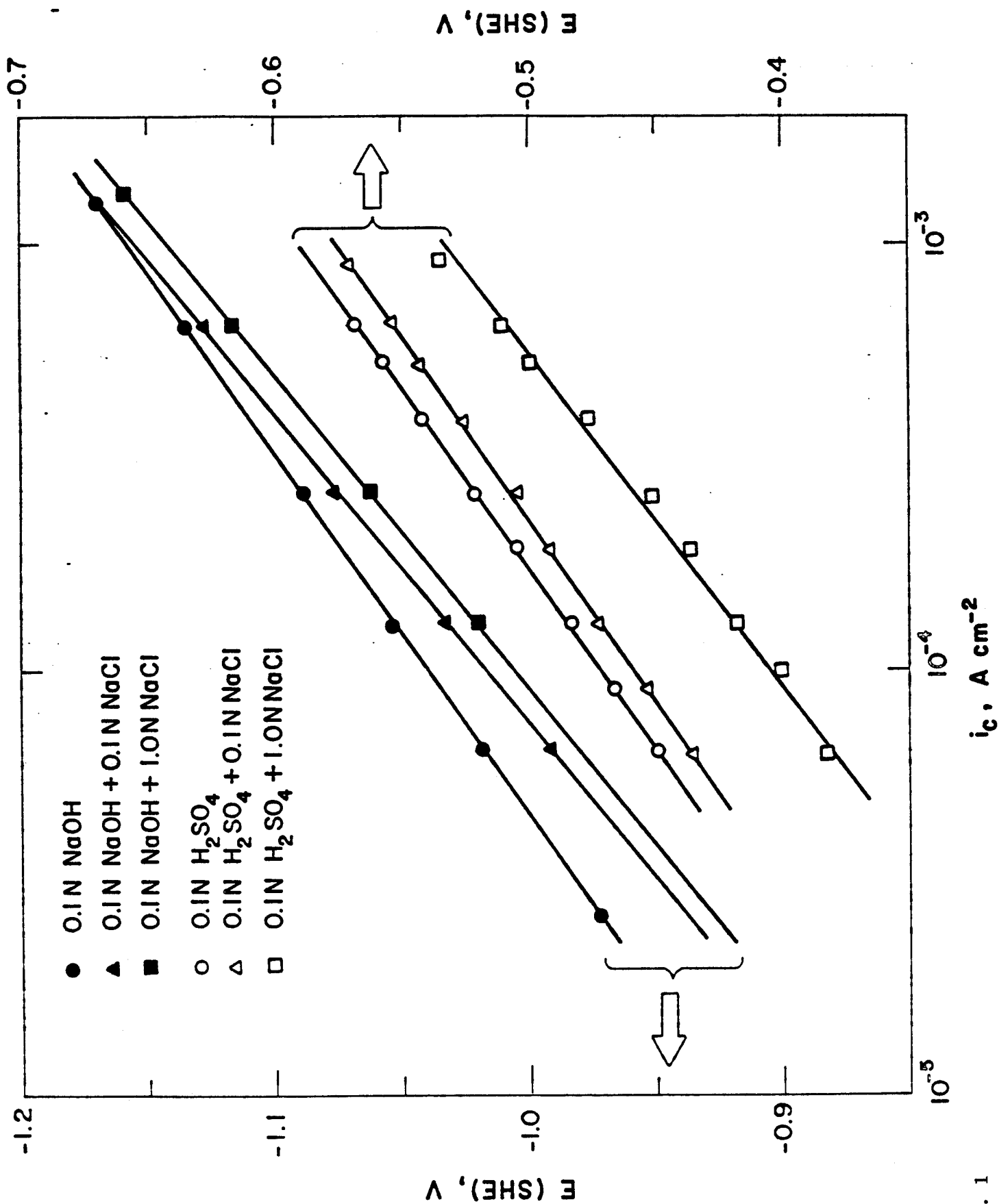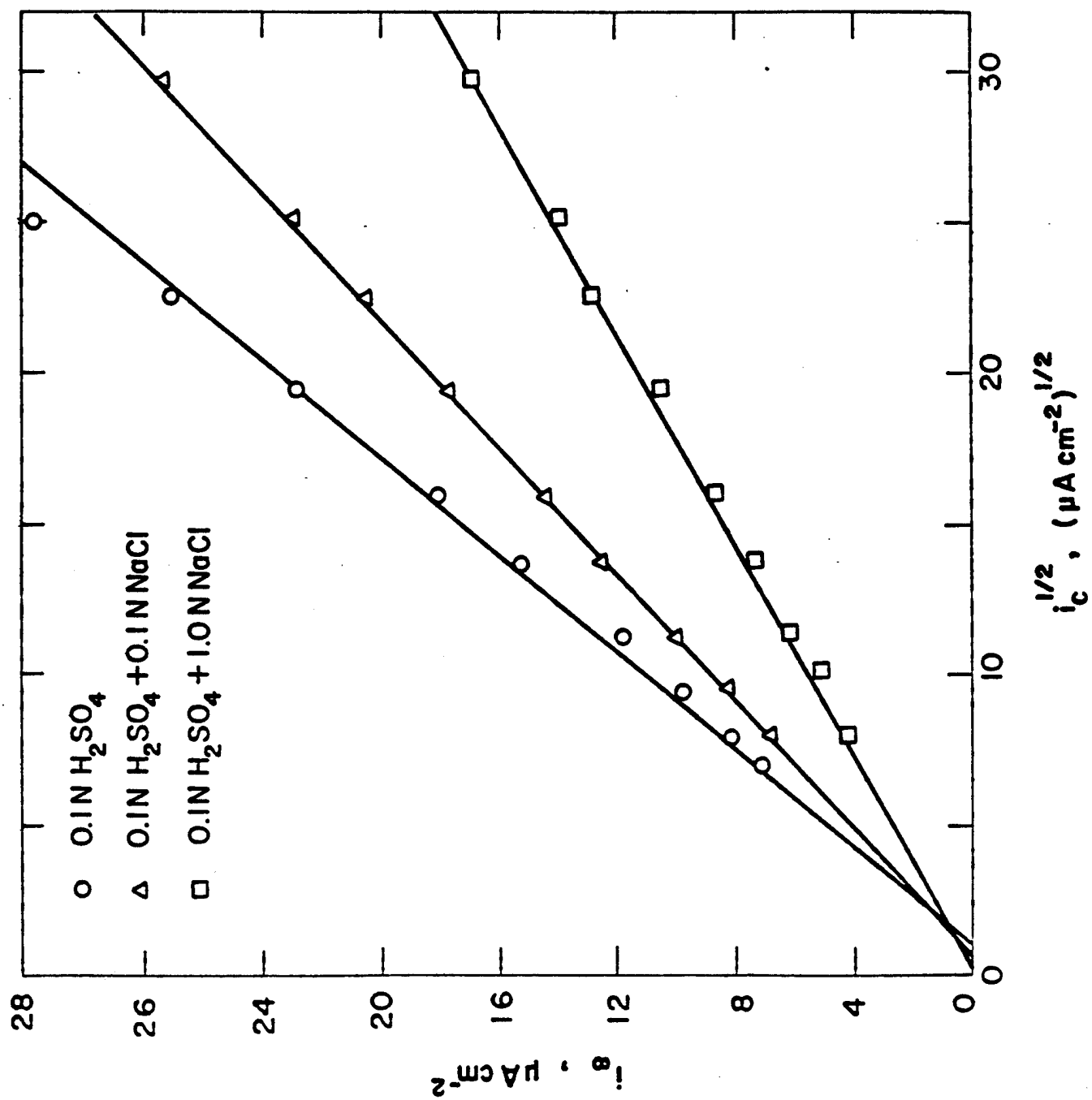
E (SHE), V

E (SHE), V

i_c , A cm^{-2}

● 0.IN NaOH
▲ 0.IN NaOH + 0.IN NaCl
■ 0.IN NaOH + I.0N NaCl
○ 0.IN H$_2$SO$_4$
△ 0.IN H$_2$SO$_4$ + 0.IN NaCl
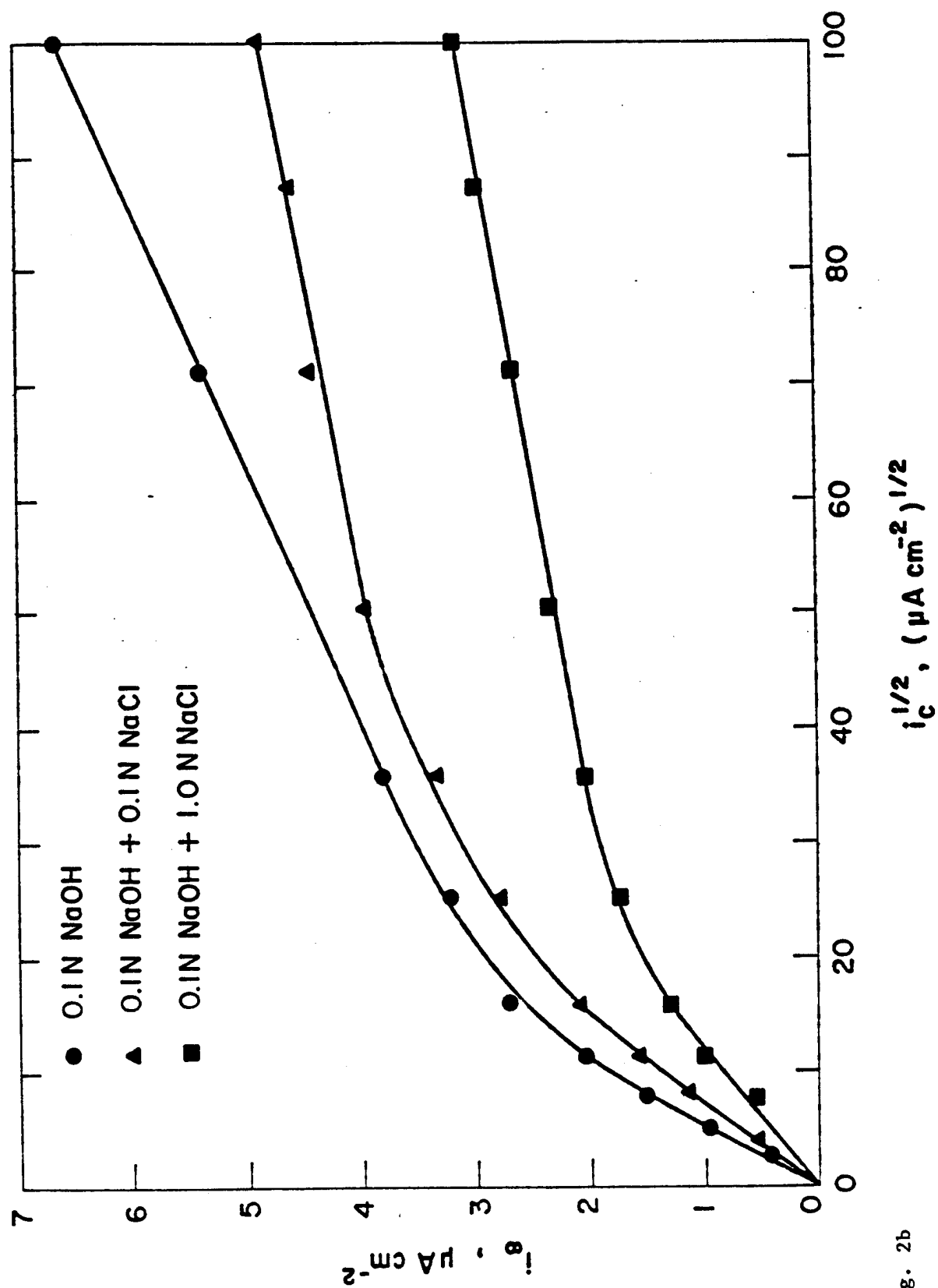□ 0.IN H$_2$SO$_4$ + I.0N NaCl
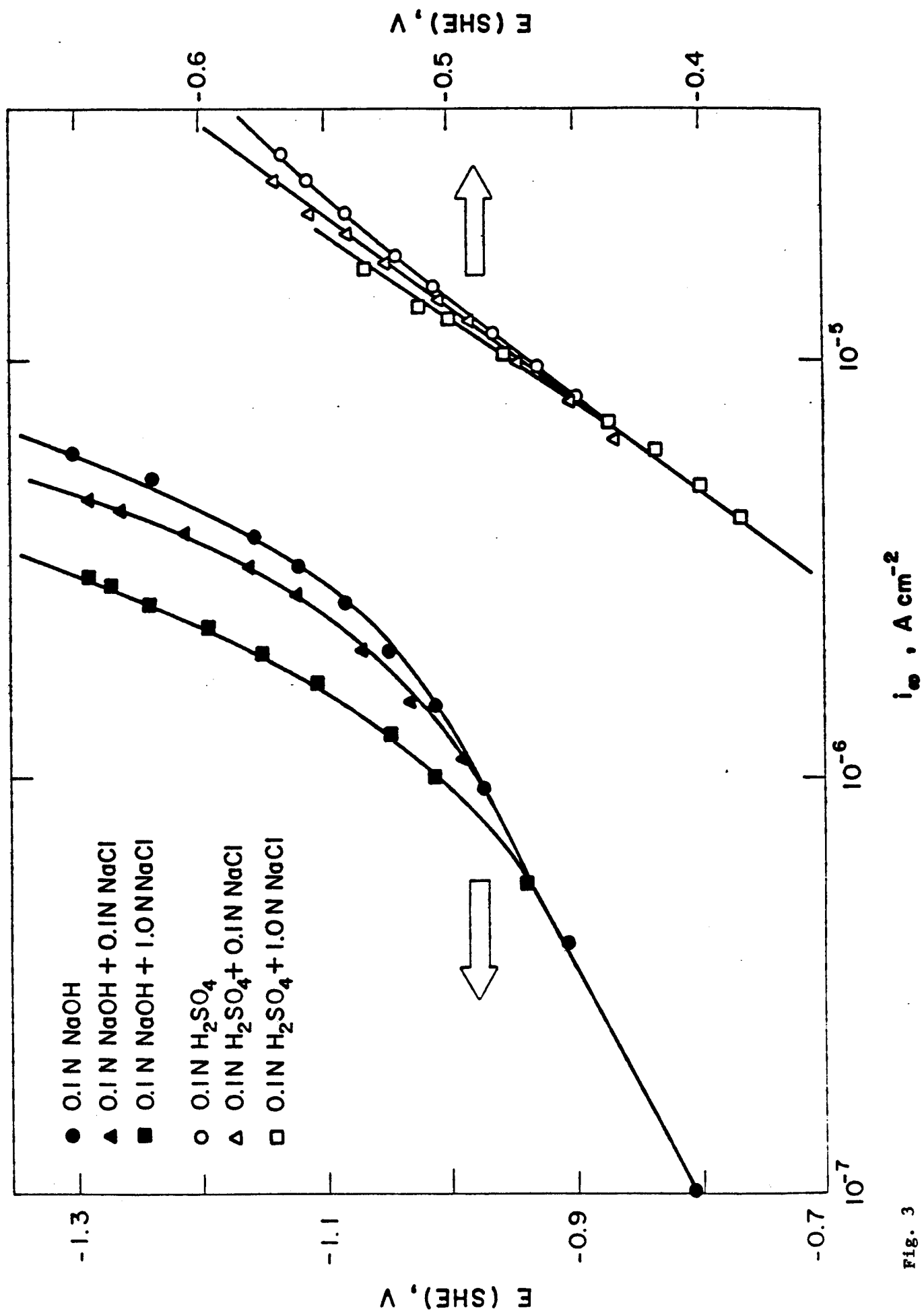
Fig. 1

Fig. 2a

Fig. 2b

Fig. 3

Pergamon

0010–938X(95)00024-0

THE DISTRIBUTION OF ANODIC AND CATHODIC REACTION SITES DURING ENVIRONMENTALLY ASSISTED CRACKING

B.G. ATEYA* and H.W. PICKERING

Department of Materials Science and Engineering, The Pennsylvania State University, University Park, PA 16802, U.S.A.

Abstract—This paper treats the effects of charge and mass transport limitations on the distribution of cathodic and anodic reactions on the flanks of environmentally assisted cracks. Under conditions of cathodic protection of the metal surface, it is shown that the presence of recesses or cracks leads to significant changes in the potential and ionic concentrations at various distances into the cavity. Consequently, the rate of the hydrogen evolution reaction decreases with increasing distance into the cavity. For active metals, e.g. Fe or Ni, metal dissolution occurs with progressively increasing rates at increasing distance into the crack. The variations of these cathodic and anodic current distributions with distance within the crack (or with the time of cracking) depends on the dimension of the opening of the crack a, the diffusivity of the hydrogen ion, D_{H^+}, and, hence, the conductivity of the electrolyte, and the polarization at the external surface of the metal, $\eta(0)$. Analysis of the migration–diffusion problem leads to the development of a characteristic depth given by

$$Z = \left[\frac{FD_{H^+} c^0_{H^+} a}{i_0 H} \exp\frac{(\beta\eta(0))}{b} \right]^{1/2} \text{ cm,}$$

where $c^0_{H^+}$ is the acid concentration, and β and i_0 are the charge transfer coefficient and the exchange current density of the hydrogen evolution reaction, respectively. Z has a strong effect on the behavior of the system.

INTRODUCTION

The mechanism of environmentally induced cracking of metals and alloys is attracting ever-increasing attention. Several conference proceedings and review articles have been published[1–3] which review the literature and project the present state of understanding of this issue. The phenomenon necessarily involves complex interactions between the prevailing environment and the electrode potential at the alloy surface with its microstructural features under the effects of stress. It is now widely recognized that the chemical and electrochemical conditions within cavities or cracks (and actually at the tip of such cracks) in metals and alloys are different from those at the external surface.[4–6] Over the years, this recognition led to the evolution of a general belief that the anodic and the cathodic reactions are spatially separated, i.e., when the anodic reaction occurs within a pit, crevice or a crack, the cathodic reaction occurs at the outer surface and vice versa. This assumption has been frequently used in modeling the cracking and pitting processes.[7–9] It will be shown below that well-separated anodic and cathodic reactions is only a limiting case which is encountered in

early stages of crack growth. The general case for base metals involves distributions of both the anodic and cathodic (hydrogen evolution) reactions, with various intensities at different locations on the internal surfaces of the cracks, along with the reduction of an oxidant at the outer surface for the special case of a freely corroding metal. This more complicated situation is a result of the combined effects of the potential distribution (IR) down the crack and the polarization characteristics of the particular system. It is also shown that at a later stage of cracking in active (base) metals, the situation might well reach the other limit, i.e. where both the anodic and cathodic (hydrogen evolution) reactions occur simultaneously at the same place and at the same rate deep within the crack, under a mixed potential established by the particular metal/hydrogen evolution system existing inside the crack.

The objective of this paper is to present and explore the relations which govern the distributions of anodic and cathodic reactions on the internal surfaces of cracks that propagate inward from the sample surface, and the dependence of these distributions on crack geometry, the electrochemical parameters of the system. the properties of the prevailing environment and the electrode potential at the alloy surface. These distributions are shown to vary with the time of propagation of, and the distance within, the crack.

Potential drop within cracks: causes and consequences.

When a cracked metal surface is held under a certain electrode potential, $E(0)$, the flanks of the crack are usually under different local values of electrode potential, $E(x)$, where x is the distance into the crack. Figure 1 illustrates this situation, for a rectangular crack.[10] The magnitude of the potential difference is given by

$$\Delta E(x) = E(0) - E(x) = \varphi(x), \tag{1}$$

where $\phi(x)$ is the local galvani potential difference in the electrolyte which fills the crack, i.e. $\phi(x) = 0$ at $x = 0$. The magnitude and sign of $\Delta E(x)$ depend on the distance down the crack x, the crack opening a, the magnitude and sign of the current density at the outer surface (i_s) supported by the potential at the outer surface, $E(0)$, and the resistivity of the electrolyte path from $x = 0$ to x. This potential difference occurs in the electrolyte phase. It drives the ionic current through the resistivity of the electrolyte path within the crack. This ionic current is equivalent to the sum of the faradaic currents which result from the electrochemical charge transfer reactions occurring on the flanks of the crack. The magnitude of this potential difference is given by

$$\varphi(x) = \int_0^x I(x)\rho(x)\mathrm{d}x, \tag{2}$$

where $I(x)$ is the local ionic current density flowing in the x direction through the electrolyte that fills the crack, and $\rho(x)$ is the local resistivity of the electrolyte path at x. The relation between $E(x)$ and $E(0)$ is given by:

$$E(x) = E(0) - \int_o^x I(x)\rho(x)\mathrm{d}x \tag{3}$$

Equation (3) is written such that the ionic current density I has a positive sign for anodic currents and a negative sign for cathodic currents. The consequences of equation (3) can be far-reaching, depending on the magnitude of the IR term. For

instance, under the local potential value of $E(x)$, one or the other of the following possibilities occur:

1. The current density $i(x)$ on the flanks of the crack, representing the rate of the half cell reaction occuring at x, becomes significantly different (up to an order of magnitude) from that at the external surface, i_s, under $E(0)$. The local current density $i(x)$ may be greater or smaller than i_s at the outer surface, depending on the particulars of the system.

2. For cracks in active metals, e.g. Fe or Ni, another electrochemical reaction takes place if favored by its polarization behavior and the local value of $E(x)$. In that respect, if the crack tip is under a potential $E(x)$, it might well encounter electrochemical reaction(s) different in nature and rate than those occurring at the outer surface of the metal.

Some of the governing equations are presented below and are used to illustrate the distributions of anodic and cathodic reaction rates at different distances within cracks under cathodic polarization conditions. The effects of crack geometry (aspect ratio, La^{-1} in Fig. 1), extent of polarization, and the transport properties of the electrolyte on these distributions, will be illustrated and discussed.

The test system

The discussion is presented below for a system of iron in sulfuric acid, for which the computed polarization curve is shown in Fig. 2(a). This figure was constructed using the following rate equations for both the metal dissolution and the hydrogen evolution reactions (HER) for:

$$Fe_{(s)} \rightarrow Fe^{2+}_{(aq)} + 2e^-$$ (4)

$$i_{Fe} = i_{0Fe}[\exp(\alpha n\eta(Fe)/b) - \exp(-(1-\alpha)n\eta(Fe)/b)],$$ (5)
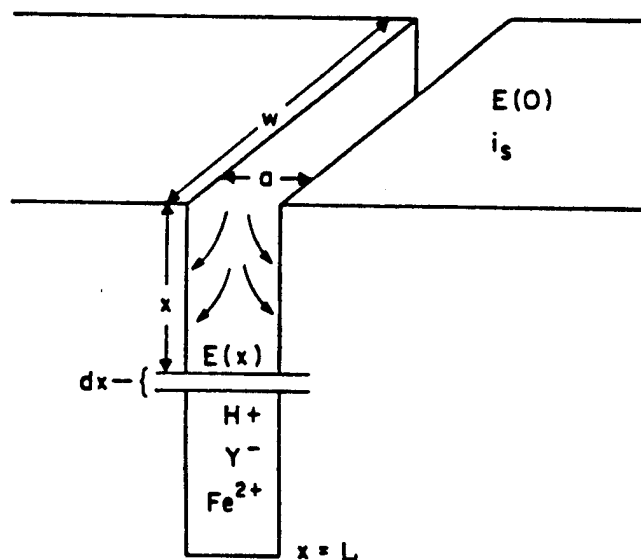

Fig. 1. Model of a crack in which the HER occurs on the outer surface (i_s) and on the crack walls. The bulk electrolyte is H^+ and Y^- and the outer $(x = 0)$ surface conditions are $E(0)$ and i_s.
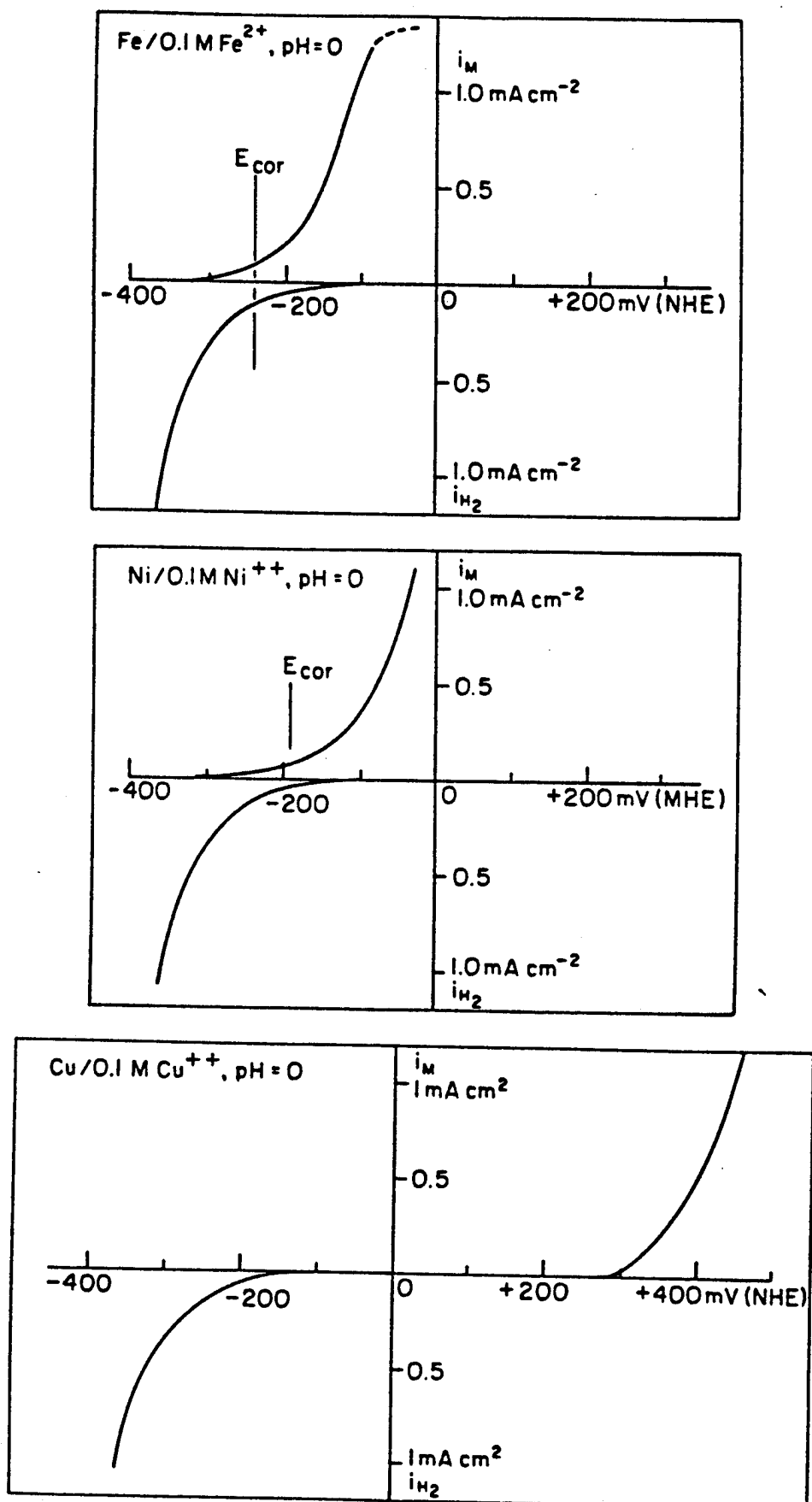
Fig. 2.   Illustration of the partial anodic and cathodic currents for the system: (a) Fe/0.1M

where i_{Fe} is the metal dissolution current per unit of metal surface area, $\eta(Fe)$ is the polarization driving the metal dissolution reaction, $b = RT/F$ and α, n and i_{oFe} are the charge transfer coefficient, the number of electrons and the exchange current density of this reaction, respectively. For the hydrogen evolution reaction, i.e.

$$2H^+ + 2e^- \rightarrow H_2(g), \qquad (6)$$

the rate is given by

$$i_H = i_{0H}[\exp(-\beta\eta(H)/b) - \exp(-(1-\beta)\eta(H)/b)], \qquad (7)$$

where i_H, i_{0H}, β, and $\eta(H)$ refer to the current density, exchange current density, charge transfer coefficient and the overpotential (polarization) driving the HER. The polarization curves in Fig. 2 were computed using typical values, i.e. $i_{0Fe} = i_{0H} = 10^{-6}$ A cm^{-2}, $b = \alpha n = 0.5$ and E_{rev} (Fe/Fe^{2+}) $= -0.470$ V(NHE) which corresponds to 0.1 M Fe^{2+} ions. The E_{rev} (H$_2$/H$^+$) was taken to be 0.0V (NHE), i.e. pH $= 0$. With this form of equations (5) and (7), the cathodic polarization has a negative sign while the anodic has a positive sign. Note that there is a fairly broad region of potential over which reactions (4) and (6) occur simultaneously albeit at different rates. In principle, this range extends from E_{rev}(Fe/Fe^{2+}) to E_{rev}(H$_2$/H$^+$), i.e. from -470 mV (NHE) to 0 mV (NHE). The free corrosion potential of this system is the potential at which both the anodic metal dissolution and cathodic hydrogen evolution currents are equal.[11]

The corresponding situations for Ni and Cu are shown in Figs 2(b) and 2(c). For Ni the potential range over which both nickel dissolution and hydrogen evolution occur simultaneously (from -280 to 0 mV) is much less than in the case of Fe. The case of Cu represents a limit in that both the anodic copper dissolution and cathodic hydrogen evalution reactions cannot occur simultaneously. In fact, they are separated by about 350 mV on the potential coordinate. These figures will prove to be most useful in a discussion of the significance and consequences of potential shifts within cracks.

Transport equations

A model system of a rectangular crack in an iron surface exposed to a dilute acid solution is considered. Allowance is made for one-dimensional mass transport by diffusion and ionic migration in the x-direction into the crack. The transport relations of dilute electrolytes are used. No allowance will be made here for the additional effects of hydrolysis (localized acidification) or complexation of metal ions, gas bubbles, formation of salt film, etc. However, an important factor which has been frequently ignored is allowed for, i.e. the distribution of the electrochemical reactions on the walls of the crack. The equations are formulated assuming a pseudo-steady state. This assumption is justified in view of the following order of magnitude calculation. Let us consider that the crack propagates 1 cm in 10^7 s. Then, taking an average diffusivity of ions within the electrolyte of $D \simeq 10^{-5}$ cm^{2}s^{-1}, the root mean square displacement during this time is $\sqrt{x^2} \simeq \sqrt{2 \times 10^{-5} \times 10^7} \simeq 14$ cm. Thus, the rate of mass transfer $(14 \times 10^{-7}$ cm s$^{-1})$ is much faster than that of crack propagation for values of the crack propagation speed lower than 10^{-7} cm s^{-1}.

Performing a mass balance, on the various ionic species, on a space element dx, as shown in Fig. 1, one obtains

$$J_{H^+} = -D_{H^-} \left[\frac{dc_{H^+}}{dx} + c_{H^-} \frac{F}{RT} \frac{d\phi}{dx} \right] = \frac{I_{H^+}}{F} . \tag{8}$$

$$j_{y^-} = -D_{y^-} \left[\frac{dc_{y^-}}{dx} - c_{y^-} \frac{F}{RT} \frac{d\varphi}{dx} \right] = 0, \tag{9}$$

$$j_{Fe^{2+}} = -D_{Fe^{2+}} \left[\frac{dc_{Fe^{2+}}}{dx} + 2c_{Fe^{2+}} \frac{F}{RT} \frac{d\varphi}{dx} \right] = -\frac{I_{Fe^{2-}}}{2F} . \tag{10}$$

where the j symbols refer to the ionic fluxes through the electrolyte in the crack as a function of distance x, c and D refer to the concentration and diffusivity, respectively, of the various ionic species and φ is the potential drop into the crack (equation (1)). With this formulation of the problem, it follows that $\varphi > 0$ for anodic polarizations and $\varphi < 0$ for cathodic polarizations. All the variables in equations (8)–(12), i.e. the c, I and φ variables, are functions of distance, x. The concentration terms are also subject to the electroneutrality condition, i.e.,

$$c_{H^+} + 2c_{Fe^{2+}} = c_{y^-} . \tag{11}$$

These fluxes are supported by the electron transfer reactions taking place on the flanks of the crack. The rates of these reactions are related to the local value of electrode potential and the electrode kinetics of the particular reaction by the Butler-Volmer equation. Considering the space element, dx in Fig. 1. one obtains

$$\begin{aligned} dI_{H^+} &= \left(\frac{2}{a}\right) i_H(x) dx \\ &= \left(\frac{2}{a}\right) i_{0H} [\exp(-\beta\eta(H)/b) - \exp(-(1-\beta)\eta(H)/b)] dx \end{aligned} \tag{12}$$

and

$$dI_{Fe^{2+}} = \left(\frac{2}{a}\right) i_{0Fe}[\exp(\alpha n\eta(Fe)/b) - \exp(-(1-\alpha)n\eta(Fe)/b)] dx, \tag{13}$$

where I_{H^-}, β and $\eta(H)$ are, respectively, the ionic current density resulting from the flow of H^+ ions within the electrolyte that fills the crack in the x direction (Fig. 1), the charge transfer coefficient of the HER and the polarization driving the HER. Similarly, I_{Fe2+}, α and $\eta(Fe)$ are the corresponding parameters for the metal dissolution reaction. The polarizations, $\eta(H)$ and $\eta(Fe)$, are given by

$$\eta(H) = E(0) - \varphi(x) + 0.059pH, \tag{14}$$

$$\eta(Fe) = E(0) - \varphi(x) - E_{rev}(Fe/Fe^{2+}). \tag{15}$$

where the E_{rev} (Fe/Fe^{2+}) is the reversible potential of iron in the particular medium.

The boundary conditions of the system are defined in terms of ionic concentrations and current or potential at the external surface. Thus, at $x = 0$,

$$c_{Fe^{2+}} = 0, c_{y^-} = c_{H^+} = c^o \tag{16}$$

and at $E(0)$,

$$i_H \text{ and } i_{Fe} = f(\text{polarization curves}). \qquad (17)$$

There are now six equations [(9)–(14)] and six variables (C_{H+}, c_{y-}, $c_{Fe^{2-}}$, I_{H-}, $I_{Fe^{2+}}$ and ϕ).

The literature has no reference to a complete solution to this system of equations. Solutions for various limiting cases have been reported. Several such solutions assumed passive or inert flanks of the cracks. They ignored the distribution of the electrochemical reactions on these flanks.[7-9] Some of the solutions are presented below which allow for these distributions, albeit for some limiting cases. In order to bring out the physical significance of, and the inter-relationships among, the various parameters and variables of the system, the cases where analytical solutions to the equations were obtained are discussed.

Cathodic polarization

Under conditions of cathodic polarization of the external metal surface at a potential $E(0)$ which supports a cathodic current (i_s) at the outer surface, and assuming that only the HER is taking place within the crack, the system is governed only by equations (8) and (9). An analytical solution to this system is available in the literature.[10] The potential, ionic concentration and current distributions are given by:[10]

$$\phi(x) = \frac{RT}{F} \ln \frac{\cosh[(L-x)Z]}{\cosh[L/Z]}, \qquad (18)$$

$$c(x) = c^o \frac{\cosh[(L-x)/Z]}{\cosh[L/Z]}, \qquad (19)$$

$$i(x) = i_s \frac{\cosh[(L-x)/Z]}{\cosh[L/Z]}, \qquad (20)$$

where L is the crack depth and Z (in cm) is a characteristic depth given by

$$Z = [FD_{H^+} \cdot c_{H^+}^o \cdot a/i_s]^{1/2}. \qquad (21)$$

Note that the characteristic depth Z includes the system parameters relating to: (i) the electrode kinetics and potential driving the HER (via i_s and equation (7)), (ii) the width of the crack opening a, which determines the aspect ratio $L\,a^{-1}$, (iii) the concentration and the diffusivity of hydrogen ions in, and conductivity of, the electrolyte (via the product $D_{H+} \cdot c_H^0 \cdot F$). It will be shown below that the characteristic depth Z determines the behavior of the system. Note also that the current i_s is related to the potential $E(0)$ at the external surface of the metal through equation (7). Upon substituting for i_s from equation (7) (assuming the polarization is sufficiently large to ignore the reverse reaction), one obtains

$$Z = \left[\frac{FD_{H^+} \cdot c_H^0 \cdot a}{i_{0H}} \exp \frac{(\beta\eta(0))}{b} \right]^{1/2} \text{cm}. \qquad (22)$$

Thus, a decrease in the magnitude of the crack opening dimension a and/or an

increase in the magnitude of cathodic polarization $\eta(0)$ which drives the reaction at the external surface (and which has a negative sign) lead to a decrease of the value of Z. A similar characteristic depth Z has frequently been used in studying the current distributions during the electroplating within cracks or scratches.[12]

For the sake of a quantitative calculation, let us consider the case of an iron surface cathodically protected under a potential of $- 0.5V$ (NHE) in an electrolyte solution of pH $= 3$ at $25^{\circ}C$. This value is comparable to the $-0.8V$ (Cu CuSO$_4$) which is commonly used in the practice of the cathodic protection of steel. Assuming the transfer coefficient is $\beta = 0.5$ and the exchange current density, i_0, of the HER is 10^{-8} A cm^{-2}, it follows that the value of $i_s \approx 5.5 \times 10^{-6}$ A cm^{-2}. Using values of $D_{H+} = 10^{-5}$ cm^{2}s^{-1}, $c^0 = 10^{-6}$ mol cm^{-3}, $F = 96487$ C eq^{-1} and $a = 10^{-2}$ cm, $Z = 0.042$. The current and potential distributions under various conditions for several combinations of L (from 10^{-3} to 1 cm) and Z (from 0.004 to 0.04 cm) have been calculated. The results are presented below.

Figure 3 illustrates the potential and (cathodic) current distributions within cracks of different depths ranging from $L = 10\ \mu m$ to 1 cm, for a value of characteristic depth, $Z = 0.04$ cm. The distance coordinate uses a logarithmic scale to accommodate the broad range of values of crack length. Furthermore, it gives a measure of the cracking time. Assuming a constant value of the crack propagation speed, e.g., 10^{-7} cm s^{-1}, one can easily calculate the cracking time. To that extent, the calculations give the time variations of the spatial potential and current distributions on the flanks of the crack. The pH within the crack also changes, becoming more alkaline with distance into the crack as given by equation (19). If the aspect ratio is favorable for formation of Fe^{2+} ions, the pH will rise to a limiting value which is the equilibrium pH of the hydrolysis reaction as discussed elsewhere.[13]
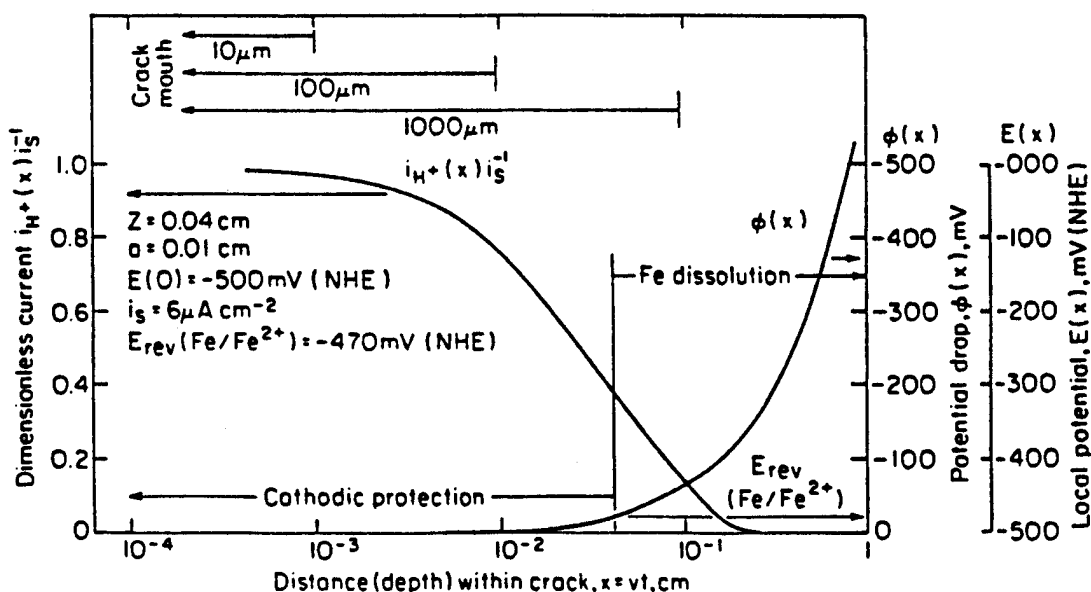

Fig. 3. Potential and HER current distributions within cracks of various depths for a value of the characteristic depth $Z = 0.04$ cm during cathodic polarization of the iron surface (see text).

Figure 3 reveals that as the distance within the crack (or the cracking time) increases, the local cathodic (HER) current density decreases while the magnitude of the galvani potential difference in the electrolyte, $\phi(x)$, increases. Since $\phi(x)$ is negative, equation (1) requires that the local electrode potential $E(x)$, shifts in the (less negative) more noble direction with increasing distance into the crack. Two potential scales are used on the right coordinate of Fig. 3; one for the IR drop in the crack electrolyte, $\phi(x)$, and the other for the local electrode potential, $E(x)$. As the distance within the crack increases (for constant Z), the magnitude of $\phi(x)$ increases (while $\phi(x)$ is negative in value), i.e., there is a greater shift of the local potential $E(x)$ in the more noble (less negative) direction. No iron dissolves as long as $E(x)$ is negative of E_{rev} (Fe/ Fe^{2+}), which is -0.470V (NHE) for the present case while hydrogen is evolved profusely under this potential. As $E(x)$ becomes equal to or positive of E_{rev} (Fe/Fe^{2+}), iron dissolution occurs along with hydrogen evolution, at rates dependent on the position of $E(x)$ on the potential coordinate in Fig. 2. As $E(x)$ shifts further towards less negative values, $i_H(x)$ decreases while $i_{Fe}(x)$ increases gradually. At the limit of $i_H(x) = i_{Fe}(x)$ the value of $E(x)$ equals the free corrosion potential of the system existing inside the crack, as shown in Fig. 2. One can easily use equations (5) and (7) to calculate $i_H(x)$ and $i_{Fe}(x)$, respectively, at various distances into the crack.

Figure 3 shows that under these conditions iron dissolution occurs at distances into the crack of $x \geq 0.04$ cm, i.e., 400 μm. Thus, for cracks of $L = 10$ or 100 μm depth under the present conditions (i.e., $a = 10^{-2}$ cm, $E(0) = -0.5$V (NHE), the entire depth of the crack will be cathodically protected (see below for $a \ll 10^{-2}$cm or $E(0) < -0.5$V (NHE)). On the other hand, for a crack of 0.1 cm depth (1000 μm), only the top 60% of its flanks will be under cathodic protection. The bottom 40% will be undergoing simultaneous anodic dissolution and hydrogen evolution at rates which are dependent on distance, as discussed above. Alternatively, for a 1 cm deep crack, only the top 4% of its depth is under cathodic protection while the rest is undergoing anodic dissolution. Using the $E(x)$ value calculated from equation (1) and a knowledge of the active/passive behavior as a function of pH, it can be determined if the anodic metal dissolution undergoes active or passive dissolution as a function of distance into the crack (or cracking time), as reported elsewhere for crevice corrosion.[14]

Figures 4 and 5 illustrate the effects of one order of magnitude decrease in Z, i.e., for $Z = 0.004$ cm. This decrease in Z was brought about in two different ways, i.e., by decreasing a from 10^{-2} to 10^{-4} cm in Fig. 4, keeping $E(0) = -0.500$V (NHE) and all other parameters constant, Fig. 4; and by changing $E(0)$ from -0.50 to -0.72 (NHE) while keeping $a = 10^{-2}$ cm and the other parameters constant, Fig. 5. For the case of $a = 10^{-4}$ cm in Fig. 4, the distance beyond which iron dissolution occurs becomes much shorter, being in this case only about 0.004 cm, i.e. 40 μm. Under this condition iron dissolution occurs at distances greater than 40 μm. Consequently, for any crack of a depth less than 40 μm (for the conditions of Fig. 4), the entire crack depth will be under cathodic protection. Similarly, for the conditions in Fig. 5, cracks will be fully protected if less than 400 μm in depth. Conversely, for a 1 cm deep crack, only the top 4% of its depth will be under cathodic protection while its interior (96% of its depth) will be involved in anodic dissolution.

For very narrow cracks ($a = 100$ Å and $E(0) = -0.5$ (NHE)) only the top 1.6 μm of cracks of any depth will be under cathodic protection, the rest being involved in anodic dissolution.
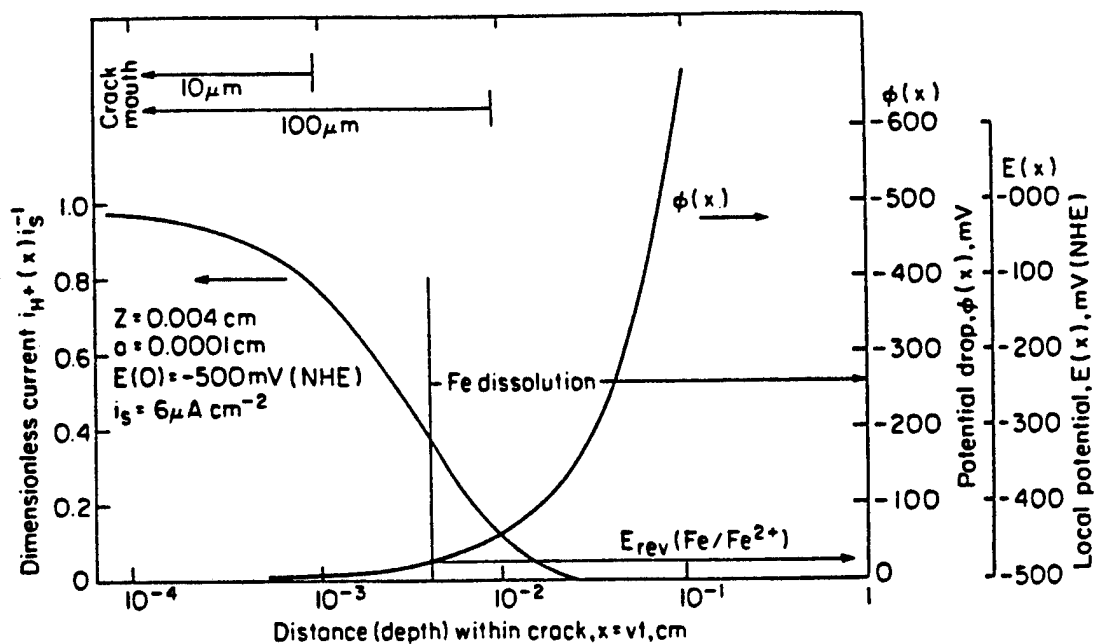
Fig. 4.   The effect of the decrease in crack opening dimesion a on the potential and current
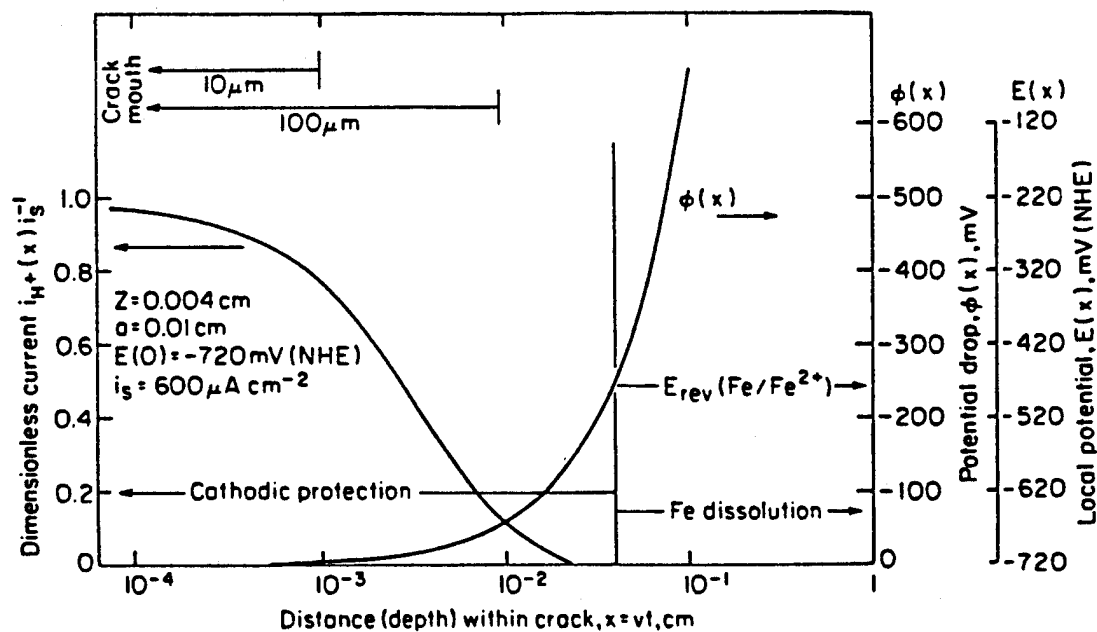distributions for the conditions in Fig. 3.

Fig. 5.   The effect of the decrease in cathodic polarization at the outer surface, $E(0)$, on the
potential and current distributions for the conditions in Fig. 3.

CONCLUSIONS

The present analysis of the diffusion–migration problem within environmentally assisted cracks leads to the following conclusions:

1. The current and potential are non-uniformly distributed within cracks. A characteristic depth Z was derived which combines the important parameters of the system, and affects these distributions,

$$Z = [\frac{FD_{H^+}c^o_{H^+}a}{i_{0H}}\exp\frac{(\beta\eta(0))}{b}]^{1/2} \text{ cm.}$$

2. For conditions of cathodic polarization at the external metal surface, the potential within the crack shifts in the noble direction towards a limiting value, as a result of the potential shift (*IR*) mechanism. The nature of this limiting value of potential is different for active than for noble metals.

3. This potential shift leads to significant decreases in the rate of hydrogen evolution on the flanks of the crack.

4. For active metals, the potential shift may become sufficiently large to promote anodic dissolution within the crack even though the external metal surface is under cathodic protection.

5. The most general case involves nonuniform distributions of both the cathodic and anodic reactions on the flanks of cracks.

6. An initial crack in an active metal may remain under cathodic protection until its aspect ratio, $L\,a^{-1}$ or depth L (for a constant opening dimension a) reaches a certain critical value when the potential at L shifts to the region of metal dissolution. This critical depth depends on the value of a, the properties of the environment and on the polarization at the metal surface through the characteristic depth Z.

REFERENCES

1. S.M. Bruemmer, E.I. Meletis, R.H. Jones, W.W. Gerberich, F.P. Ford and R.H. Staehle (ed.), *Parkins Symp. on Fundamental Aspects of Stress Corrosion Cracking*, TMS, Warrendale (1992).
2. R.P. Gangloff and M.B. Ives (ed.), *Environment-Induced Cracking of Metals*, NACE, Houston (1990).
3. R.W. Revie. *Modern Aspects of Electrochemistry* (ed. B.E. Conway, J.O'M. Bockris and R.E. White), Vol. 26, p. 277. Plenum, NY (1994).
4. A. Turnbull, *Corros. Sci.* **23**, 833 (1983).
5. Z. Szklarska-Smialowska, *Pitting Corrosion of Metals*, NACE, Houston (1986).
6. B.F. Brown, C.T. Fuji and E.P. Dahlberg, *J. Electrochem. Soc.* **116**, 218 (1969); J.A. Smith, M.H. Peterson and B.F. Brown, *Corrosion* **26**, 539 (1970).
7. D.D. Macdonald and M. Urquidi-Macdonald, *Corros. Sci.* **32**, 51 (1991).
8. J.R. Galvele, *J. Electrochem. Soc.*, **123**, 464 (1976).
9. H.W. Pickering and R.P. Frankenthal, *J. Electrochem. Soc.*, **119**, 1297 (1972).
10. B.G. Ateya and H.W. Pickering, *J. Electrochem. Soc.*, **122**, 1018 (1975).
11. C. Wagner and W. Traud, *Z. Elektrochem.* **44**, 391 (1937).
12. C. Wagner, *Plating*, **48**, 997 (1961).
13. B.G. Ateya and H.W. Pickering, *Hydrogen in Metals*, Vol 2 (ed. I.M. Bernstein and A.W. Thompson), p. 207. ASM, Metals Park (1974).
14. Y. Xu and H.W. Pickering, *J. Electrochem. Soc.* **140**, 658 (1993); Y. Xu, M. Wang and H.W. Pickering, *ibid* **140**, 3448 (1993).

Hydrogen Evolution and Absorption within Grain Boundary Grooves in Sensitized Stainless Steel under Conditions of Anodic Polarization

A. Sehgal,* B. G. Ateya,**.ª and H. W. Pickering***

Department of Materials Science and Engineering, The Pennsylvania State University, University Park, Pennsylvania 16802, USA

ABSTRACT

This paper presents evidence for the electrolytic generation of hydrogen within the grain boundary grooves of a sensitized 430 stainless steel membrane while both of the sample's outer surfaces are anodically polarized with respect to the hydrogen evolution reaction (HER). The grooves are formed by the anodic dissolution of the chromium depleted zone adjacent to the precipitated chromium carbides. Hydrogen absorption is shown to occur from within the steel using the Devanathan-Starchurski hydrogen permeation cell. This result is consistent with earlier observations of gas evolution from within grain boundary grooves. It follows that the local electrode potentials inside the grooves are considerably less noble than those applied at the outer surfaces. An IR potential shift mechanism explains the results.

Introduction

Recent studies on the formation of grain boundary grooves during anodic polarization of sensitized 430 stainless steel (430 SS) have shown that a gas forms and evolves out of the grain boundary grooves.[1,2] The formation of the gas, presumably hydrogen, was attributed to the existence of thermodynamically favorable potentials that are established by a large IR drop within the electrolyte filling the grain boundary groove.[2] In this explanation the IR drop shifts the local electrode potential within the grooves into the region of the hydrogn evolution reaction (HER).[3,4] If the gas is proved to be hydrogen, its observation can be taken as a proof of the presence of a large potential drop within the grooves. Gas has also been observed evolving out of pits[3] and crevices[4] in iron. In the pitting investigation,[3] the gas emanating from the pits was found to be hydrogen by analysis in a mass spectrometer.

The purpose of this work is to determine (*i*) whether the electrolytically produced gas within the grain boundary grooves is hydrogen and (*ii*) whether this source of hydrogen can lead to the absorption of hydrogen into the metal and its subsequent embrittle-

* Electrochemical Society Student Member.
** Electrochemical Society Active Member.
*** Electrochemical Society Fellow.
ª Permanent address: Department of Chemistry, Faculty of Science, Cairo University, Cairo, Egypt.

ment. This was done by detecting the presence of hydrogen in the metal using the Devanathan-Starchurski cell[5] with both of the membrane surfaces maintained at anodic potentials which prohibit the HER. Answers to these questions are important as they point to the possibility of hydrogen embrittlement of steels under anodic protection.

Experimental

Membranes of 430 SS [weight percent (w/o) Cr-16.46, C-0.055, Mn-0.48, Mo-0.024, N-0.017, Ni-0.32, P-0.035, S-0.004, Si-0.36, Fe-balance] were cold rolled to the desired thickness and solution annealed at 1200°C for 1 h and ice water quenched. Sensitization was induced by heating at 550°C for 2 h followed by an ice water quench.

A Devanathan-Starchurski cell[5] was used to detect any electrolytically produced hydrogen that may have entered the metal from within the grain boundary grooves. An area of 0.8 cm² of each surface of the membrane was exposed to the electrolyte. The "charging" side of the membrane (in cell 1) was anodically polarized using a potentiostat to a potential of 192 mV (NHE) in deaerated 1 $N H_2SO_4$ (pH ~ 0.36). A saturated calomel electrode was used as the reference electrode in cell 1 along with an agar salt bridge to prevent the contamination of the electrolyte with chloride ions.

The "exit" surface of the membrane (in cell 2) was coated with Pd to protect the underlying membrane and to oxidize the hydrogen which reaches this surface. An acid solution composed of 1 N H_2SO_4 + 3 × 10⁻⁴ $M K_3Fe(CN)_6$, was used in cell 2 instead of the normally used basic solution. The potassium ferricyanide was added to the "exit" solution to detect soluble ferrous ions. If the
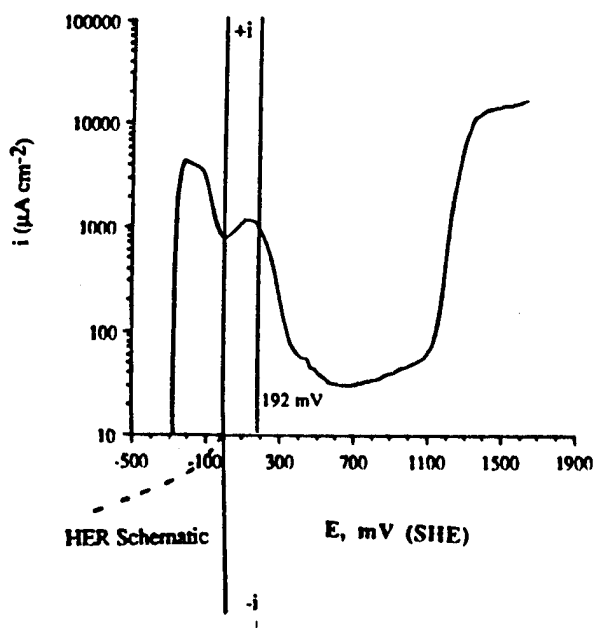

Fig. 1. Measured anodic polarization curve for sensitized type 430 stainless steel in 1 $N H_2SO_4$, and a scheme of the HER curve.
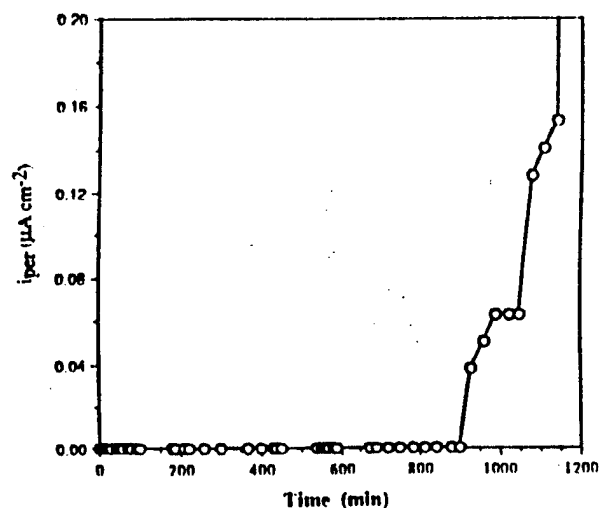

Fig. 2. Measured hydrogen permeation current at the Pd-coated "exit" surface for a membrane with both of its surfaces anodically polarized with respect to the HER. E_{cell1} = 192 mV and E_{cell2} = 642 mV (NHE).

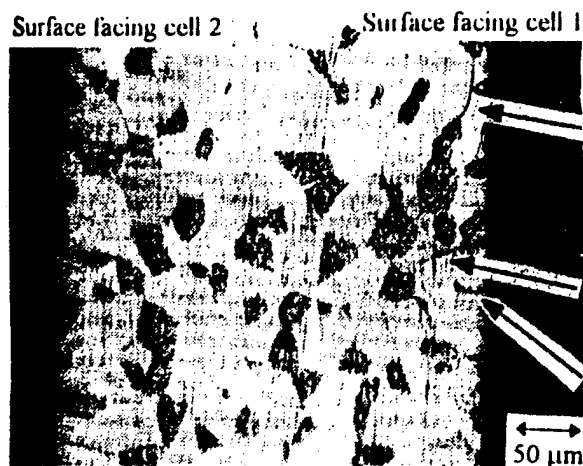Surface facing cell 2   Surface facing cell 1

Fig. 3. Cross-sectional optical micrograph showing an example of groove formation that established a sufficiently large IR drop for the occurrence of the HER inside the groove.

grain boundary grooves that form on the "charging" surface (cell 1) continue to grow, eventually penetrating the sample thickness, the iron dissolving in the groove would be detected as prussian blue spots formed by the reaction between the ferrous and ferricyanide ions.[6] The "exit" surface was continuously monitored for prussian blue spots using a mirror placed in cell 2 and a high intensity light source. A Hg/Hg_2SO_4 electrode was used to maintain the potential of the Pd-coated surface of the membrane (cell 2) at 642 mV (NHE). This value was chosen so that even if the Pd layer did not fully protect the steel, both the Cr-depleted and the bulk alloy would be passivated while ensuring complete oxidation of any hydrogen atoms arriving at the Pd-coated "exit" surface. The background currents obtained in cell 2 remained steady for up to 48 h at a level of ≤ 0.02 μA cm^{-2}. Two Wenking 75 LB M potentiostats were used to control the potentials on either side of the membrane. Purified argon gas was used to deaerate the cell compartments. The measurements were performed at 25 ± 2°C. Further details about the cell, equipment, and procedures are reported elsewhere.[7,8]

Results and Discussion

Figure 1 shows the measured anodic polarization curve of the sensitized stainless steel in 1 N H_2SO_4. The figure shows a secondary anodic maximum just to the left of the 192 mV (NHE) applied potential. The double peak is attributed to the superposition of two anodic currents, one from the bulk alloy (on the left) and the other from the very narrow ($<\mu m$) chromium-depleted zone along the grain boundary. The surface of the sensitized steel in cell 1 was maintained at 192 mV (NHE) in order to form the grain boundary grooves by dissolution of the Cr-depleted zones. This potential is about 200 mV more noble than the equilibrium potential of the HER in the 1 N H_2SO_4 solution. Details of the metallographic characterization of these grooves are reported elsewhere.[8]

Figure 2 shows the hydrogen permeation transient observed for a 0.037 cm thick sensitized 430 SS membrane whose surface in cell 1 was anodically polarized at 192 mV (NHE). Three different stages can be identified in the transient. In the first stage, that lasted about 900 min, no permeation current could be detected, as we measured only a steady background current of ~0.02 μA cm^{-2}. The duration of this stage is normally defined as the breakthrough time, beyond which hydrogen permeation is detected. In the second stage, that lasted ~270 min, a small net permeation current was detected. In the final stage the permeation current showed an exponential increase. During the first and second stages no prussian blue spots were observed on the "exit" surface. A localized blue spot became visible on the Pd-coated membrane surface in cell 2 during the final stage of the transient at 1170 min. The general behavior shown in Fig. 2 was observed in more than 10 samples, with thicknesses of 0.037 or 0.055 cm. Both the breakthrough time and the time to observe the blue spot increased considerably for the thicker membrane. Example times obtained for the 0.055 cm thick membrane amounted to 2460 and 3700 min, respectively. These are to be compared with 900 and 1170 min for the 0.037 cm thick membrane.

Figure 3 shows a cross-sectional micrograph of another membrane (0.037 cm thickness) polarized at 192 mV (NHE) in cell 1.

The experiment was stopped after a net permeation current of 0.05 μA was recorded in cell 2. It is clear that the grain boundary grooves that form on the surface in cell 1 penetrate only part of the thickness of the membrane. The deepest grain boundary grooves observed in other regions of this sample extended approximately halfway across the thickness of the membrane. No blue color was observed on the "exit" surface in cell 2 during the test. This is consistent with the observation that the grain boundary grooves extended only part way through the sample thickness at the time the test was discontinued. This micrograph is typical of all of the samples in which the experiment was interrupted during the second stage of the transient except that the depth of the penetration of the grain boundary grooves varied from sample to sample, being deeper the longer the time of the test.

The permeation transient shown in Fig. 2 is substantially different from those normally recorded under conditions of cathodic hydrogen charging of the external surface of a membrane,[5,7] where one obtains an s-shaped curve with a diffusion limited plateau. Under such conditions, the breakthrough time is given by[5] $t_b = L^2/15.3D$. Taking a value[9] of $D \sim 10^{-8}$ cm^2 s^{-1}, and $L = 0.037$ cm, one obtains $t_b \cong 150$ min. This value is much shorter than the 900 min measured in Fig. 2, which indicates that hydrogen permeation through the membrane is faster than the propagation of the grooves. The progressively increasing rate of hydrogen permeation in Fig. 2 points to the generation of hydrogen at ever increasing penetrations and surface areas within the grain boundary grooves. As the grooves penetrate deeper into the membrane thickness, the hydrogen generated and absorbed within the steel has to diffuse a shorter distance to reach the Pd-coated surface and be detected.

The breakthrough time observed in region 1 is the sum of two components associated with the various processes forming the operating mechanism, i.e., (i) The time required to dissolve the Cr-depleted zone and to generate grain boundary grooves of sufficient depth-to-opening dimensions (aspect ratio) to set up sufficiently large ohmic potential drops within the grooves so that the HER and hydrogen absorption could take place[10] and (ii) The time taken for the hydrogen absorbed in the metal lattice to diffuse from the location where it was absorbed (within the grain boundary groove, cell 1) to the Pd coated "exit" surface of the membrane where it is oxidized (cell 2). The above components of this breakthrough time cannot be easily separated, even though each of them is associated with a distinct process.

The above results indicate that hydrogen is generated within the grain boundary grooves even though the external surface of the sample is about 200 mV more noble than the equilibrium potential of the hydrogen evolution reaction in the bulk electrolyte. The actual potential drop through the electrolyte filling the grooves is greater than 200 mV in view of the resulting changes in the composition of the electrolyte within the grooves. It must be noted that great care was taken to exclude Cl$^-$ ions from the system. For bulk electrolytes of pH values >2, localized acidification occurs within the groove as a result of the hydrolysis of the metal ions produced by the reaction, which maintains the pH at about 2.[2] On the other hand, for more acidic bulk electrolytes (pH <2), the potential gradient prevailing within the grooves requires a decrease in the acid concentration (an increase in pH) inside, than outside, the groove.[3,11] The limiting value of the pH within the groove is about 2 as determined by the hydrolysis of the metal ions.[2] This difference in pH (from the bulk solution value) shifts the equilibrium potential of the HER by ~100 mV in the less noble direction. Consequently, the actual IR drop needed to cause the HER to occur within the grooves is >300 mV. This magnitude of IR drop is in agreement with IR drops that have been reported for highly constricted regions, filled with highly conducting electrolytes.[10-15] Other results showing comparable or even greater potential drops in the grain boundary groove(s) observed in this work are reported elsewhere.[8,16]

An estimate of the potential drop in the present system, using the results of measurements and modeling[10,17] of the potential distribution within constricted regions, supports the above mentioned magnitude of IR drop. From SEM micrographs[8] of the steel surface polarized at 192 mV, the opening dimension of the grooves was measured. From the model[10,17] a potential drop of 300 mV in 1 N H_2SO_4 requires an aspect (depth/opening) ratio of about 2.5 for the size of the active peak in Fig. 1. Greater potential drops are obtained in electrolytes of greater resistivity, larger active peak size and/or in cavities of larger aspect ratio, i.e., greater depth or narrower opening.[10,13] The largest opening of the grooves in the present work is of the order of microns and some of the grooves penetrated halfway through the sample thickness, i.e., 0.018 cm. This corresponds to an aspect ratio of about 180, which is far

greater than the 2.5 aspect ratio required for a potential shift of 300 mV for this particular metal/electrolyte system. This indicates that an IR drop of 300 mV occurs for a much smaller depth than 0.018 cm. The possibility of constrictions of the current path caused by gaseous or solid reaction products within the groove would effectively decrease the opening dimension and produce a 300 mV potential drop at an even shallower depth.

Conclusions

1. The detection of a hydrogen permeation current from samples whose outer surfaces were potentiostated at anodic potentials proves that the local electrode potential inside the anodically produced grain boundary grooves had shifted more than 300 mV in the less noble direction into the potential regime of the HER. Furthermore, this result demonstrates that the occurrence of the HER within the groove can lead to the absorption of hydrogen into the metal, which is a precursor to hydrogen embrittlement.

2. The grooves form by the dissolution of the chromium depleted zone adjacent to the precipitated chromium carbides in the sensitized stainless steel. For a depth-to-opening dimension (aspect ratio) of the grain boundary groove that produces a sufficiently large IR drop,[10] both the HER and hydrogen absorption occur at that depth. The absorbed hydrogen diffused to the outer surfaces including the "exit" surface (cell 2) where its arrival was detected by the oxidation current in cell 2. The formation of the grooves contributed to the measured breakthrough time for arrival of the internally generated hydrogen at the "exit" surface of the membrane.

Acknowledgment

REFERENCES

1. B. W. Bennett and H. W. Pickering, *Metall. Trans. A*, **18A**, 1117 (1987).
2. W. Kelly, R. N. Iyer, and H. W. Pickering, *This Journal*, **140**, 3134 (1993).
3. H. W. Pickering and R. P. Frankenthal, *ibid.*, **119**, 1297 (1972).
4. K. Cho and H. W. Pickering, *ibid.*, **137**, 3313 (1990); *ibid.*, **138**, L56 (1991).
5. M. A. V. Devanathan and Z. Stachurski, *Proc. R. Soc.*, **A270**, 90 (1962).
6. D. A. Skoog and D. M. West, *Analytical Chemistry*, 3rd ed., p. 466, Saunders College Publisher, Philadelphia, PA (1980); P. Hersch, J. B. Hare, A. Robertson, and S. M. Sutherland, *J. Appl. Chem.*, **11**, 246 (1961).
7. S. S. Chatterjee, B. G. Ateya, and H. W. Pickering, *Metall. Trans.*, **9A**, 389 (1978).
8. A. Sehgal, Ph.D. Thesis, The Pennsylvania State University (1995).
9. J. O'M. Bockris, M. A. Genshaw, and M. Fullenwider, *Electrochim. Acta*, **15**, 47 (1970).
10. Y. Xu, M. Wang, and H. W. Pickering, *This Journal*, **140**, 3448 (1993); Y. Xu and H. W. Pickering, *ibid.*, **140**, 658 (1993).
11. B. G. Ateya and H. W. Pickering, *J. Appl. Electrochem.*, **11**, 453 (1981).
12. I. J. Yang, *Corrosion*, **49**, 576 (1993).
13. B. G. Ateya and H. W. Pickering, *This Journal*, **122**, 1018 (1975).
14. A. Turnbull, *Corros. Sci.*, **23**, 833 (1983).
15. Z. Szklarska-Smialowska, *Pitting Corrosion of Metals*, NACE, Houston (1986).
16. A. Sehgal, B. G. Ateya, and H. W. Pickering, In preparation.
17. M. Wang, H. W. Pickering, and Y. Xu, *This Journal*, **142**, 2986 (1995).

Potential Distribution, Shape Evolution, and Modeling of Pit Growth for Ni in Sulfuric Acid

Minghua Wang and Howard W. Pickering*

*Department of Materials Science and Engineering, The Pennsylvania State University,
University Park, Pennsylvania 16802, USA*

Yuan Xu*

Singapore Institute of Standards and Industrial Research, Singapore 0511

ABSTRACT

Growth of artificial pits in the Ni/sulfuric acid system was investigated using a microprobe technique for the potential monitoring and pH measurements within the pits, as well as routine electrochemical, solution analysis, and metallographic techniques. The measured data and the observed changes in shape of the pit with time demonstrate that the IR voltage drop mechanism of localized corrosion operates for this system. Experimental results are in good agreement with the results of mathematical modeling. It is also found that the increase in Ni** ions and in pH within the pit have a destabilizing effect on the pit growth process and that this effect can be explained within the framework of the IR voltage drop mechanism.

Introduction

In our previous work on the crevice and pitting corrosion of iron,[1-7] the voltage drop (IR) mechanism was proven beyond a reasonable doubt to operate in localized corrosion. Some data were also presented which indicated how the IR concept coupled with a change in the polarization curve could explain the roles of pH, chloride ion, and inhibitor ions (chromate) in modifying the tendency for localized corrosion.[3-5] The basic feature of the IR mechanism is that the local electrode potential inside the crevice/pit is less oxidizing than the passive value at the outer surface and is in the active region of the polarization curve of the cavity electrolyte. In this way the metal dissolves at a high rate in the crevice (pit) but only at a very low passive rate on the outer surface where the cathodic reaction occurs. This separation of anode and cathode and the existence of an active peak in the polarization curve of the cavity electrolyte enables the IR mechanism to operate.

The voltage drop framework of localized corrosion is very powerful since it can readily form the basis of predictive models. The first of these models successfully predicted susceptibility as a function of cavity dimensions for crevice corrosion[6] and for pitting corrosion in artificial pits[7] for iron in a buffered pH 4.7 solution. The models have also shown that an important consequence of an IR model is that the IR concept scales down in size so that the smallest pit at the earliest stage of pitting can have the same IR drop as a larger pit at a later stage.[7] This is a consequence of their aspect ratios (pit depth to radius) being the same.[6-9] As such the IR criterion can form the basis for the transition from metastable to stable pitting.[7]

In the present paper, experimental and mathematical modeling results are presented for the growth of artificial pits in pure nickel exposed to 1N sulfuric acid (pH 0.5) in order to study the role of the IR drop in the absence of local acidification and/or chloride ion accumulation in the pit. The results demonstrate that the IR drop mechanism is operating in the Ni/sulfuric acid system. It is also shown by the present work that the stability of the pitting process, the buildup of the corrosion products in the pit solution, specifically Ni^{2+} ions, and the pH are different for pits facing upward vs. downward. For pits facing upward the Ni** ion concentration and pH both increase. This causes the size of the active peak of the polarization curve to drastically decrease resulting in a change in the IR condition which is consistent with the observed destabilization of the pitting process with increasing time.

* Electrochemical Society Active Member.

Experimental

Nickel (99.6%) specimens of 20 × 7 × 3 mm and 20 × 10 × 3 mm were embedded in cold mount resin (Fast Cure, Metlab Corp. Niagara Falls, NY). (The nickel was dissolved in acid and analyzed by inductively coupled plasma emission spectrophotometry: Mn 0.22%, Fe 0.03%, Mg 0.03%, Si 0.03%, Cr 0.06, Cu 0.02, Ti 0.02%; Co, Al not observed, balance Ni.) Artificial pits were made by drilling holes of 1 mm diam and different depths in the specimens. In some specimens the hole was drilled through both the 7 or 10 mm Ni depth and the cold mount in order to facilitate the potential distribution measurement inside the pit. The solution used for the pitting corrosion study was 1N H$_2$SO$_4$ open to the air.

Smooth specimens from the same Ni stock were used for the measurement of the polarization curve where the current was recorded after 5 or more min at each potential (potentiostatic condition). The samples were mounted and the edges of the sample were lacquered (Stop-off Lacquer, Pyramid Plastic, Inc., USA) to eliminate any crevices between the sample and the mount. The exposed surface faced upward or sideway in the polarization curve measurement and either a large volume of electrolyte (~800 ml) or small volume (~200 ml) was used, the latter for the saturated solutions. Conversely, the sideway orientation and the large volume were used to minimize buildup of the corrosion products on the surface, simulating the situation reported below in experiments with the pit facing downward. The polarization curve measurements were conducted in three different deaerated (by prepurified grade N$_2$) solutions: 1N H$_2$SO$_4$, NiSO$_4$ saturated 1N H$_2$SO$_4$, and NiSO$_4$ saturated 0.02N H$_2$SO$_4$. In the latter two measurements excess NiSO$_4$ was present in the cell to maintain the
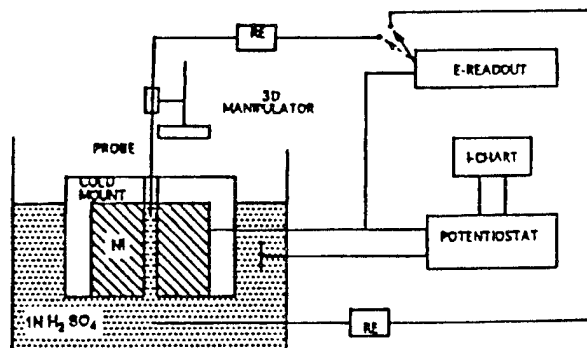

Fig. 1. Schematic diagram of the experimental setup for the artificial pit growth tests which included measurement of the potential distribution within the pit.
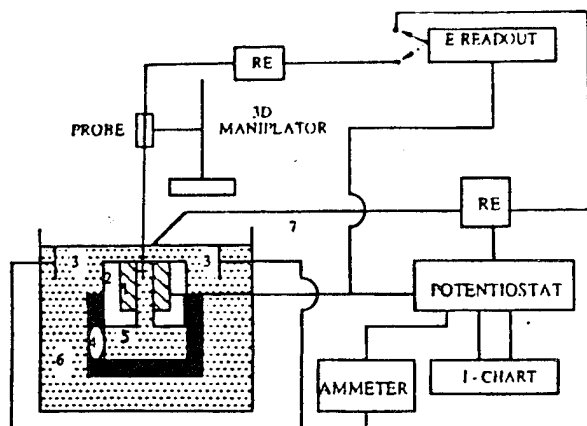
Fig. 2. Schematic of the experimental setup for the accumulation of the corrosion products during artificial pit growth: 1, Ni specimen; 2, cold mount; 3, counterelectrode; 4, PVC cylindroid; 5, electrolyte in the cylindroid; 6, electrolyte in the cell; 7, reference electrode.

saturation condition. These solutions were tested for their pH and conductivity. A pH of 0.5, 0.5, and 1.9 and conductivity of 195, 82, and 43 mS were measured for the $1N$ H_2SO_4, $NiSO_4$ saturated $1N$ H_2SO_4, and $NiSO_4$ saturated $0.02N$ H_2SO_4, respectively.

Different experimental arrangements were employed in the study. Figure 1 is a schematic of one of the experimental setups for the pitting corrosion tests in which the sample surface and pit opening face downward (upside-down orientation). A small diameter ($\gtrsim 0.2$ mm) Luggin capillary probe connected to a saturated calomel electrode (SCE) through a salt bridge containing $1N$ H_2SO_4 was used to monitor the electrode potential at different positions inside the artificial pit by entering the pit from the top opening. The diameter of the probe was always less than one-fifth of the pit diameter (1 mm) in order to minimize its resistance to current flowing out of the pit. The presence or absence of the top opening was found to have no effect on the pitting characteristics (*e.g.*, refer to Fig. 5b and c below). Another SCE connected to a potentiostat was placed close to the outer Ni (bottom) surface near the opening of the artificial pit. With the outer Ni surface polarized into the passive region (0.4 V, SCE), the measured current was essentially that due to active corrosion along the wall of the artificial pit. This upside-down arrangement of the pit enabled the more dense corrosion products to flow downward out of the pit. In addition, some experiments were run with the sample surface facing upward. These experiments are described below in connection with Fig. 2.

Figure 2 shows another experimental setup. A specimen with a hole (an artificial pit) drilled through both the Ni and the cold mount was used. The mounted specimen was inserted with the pit opening facing upward into a cylindroid filled with $1N$ H_2SO_4. This device was then put into a larger cell of $1N$ H_2SO_4 with the outer Ni surface facing upward. Its potential was held in the passive region using a potentiostat. The corrosion products moved downward and were collected in the cylindroid for analysis. In some experiments with the surface facing up, the artificial pit in Fig. 2 did not penetrate the sample thickness (so that the corrosion products would accumulate in the pit) and the cylindroid was removed. This is referred to as the right-side-up orientation.

For the upside-down orientation of the pit, pH measurements were made periodically during the experiment by withdrawing a small volume of the pit electrolyte using a syringe with a fine capillary (less than one-fifth of the 1 mm pit diameter). For the right-side-up orientation, the nickel specimen was removed from the cell at the end of the test for the pH measurement. The remaining solution on the outer surface was carefully removed by touching the edges of the surface with an adsorbent paper. Then, using the fine capillary, some of the remaining electrolyte in the pit was

extracted for analysis. This procedure minimized dilution of the cavity electrolyte. The extracted solution was then tested with pH paper.

The initial potential distributions at the onset of the pitting process inside artificial pits were calculated for the pit diameter of 1 mm using a computation model published earlier.[6,7] The computation was conducted in an IBM 3090 mainframe computer.

Results

Polarization curve.—Polarization curves of the Ni in N_2 purged H_2SO_4, with or without addition of nickel sulfate, were measured, found to be reproducible, and are presented in Fig. 3. The features of the curve are similar to those reported in the literature.[10] They all show a typical active-passive behavior, with oxygen evolution occurring at $E \gtrsim 1000$ mV SCE. There is a small plateau (shoulder) in the active region of the curve with the current increasing steeply to the peak current and dropping to the passive current at increasingly oxidizing potentials.

The three polarization curves in Fig. 3, however, are very different with respect to the size of their active loops. The polarization curve for the $1N H_2SO_4$ solution without nickel sulfate (curve a) has a peak current density of 30 mA cm^{-2} at approximately 120 mV (SCE) whereas the peak current densities for the solutions with saturated nickel sulfate (curves b and c for pH 0.5 and 1.9, respectively) are much smaller, about 3 and 0.6 mA cm^{-2}, 10 and 2% of the value for the solution without nickel sulfate, and occur at less noble potentials. The difference between curves b and c is caused by the difference in pH. Curve a was the same for both the facing up and sideway orientations, *e.g.*, the peak current density was 30 ± 1 mA cm^{-2} (mean and standard deviation of seven measurements, five sideway).

The measured open-circuit corrosion potentials were -300 and -270 mV (SCE) for nickel in deaerated $1N H_2SO_4$ and in $1N H_2SO_4$ open to the air, respectively.

Shape evolution and current distribution within the artificial pit.—A pitting corrosion test was conducted for an artificial pit of 5 mm in depth and 1 mm in diameter in the upside-down orientation (Fig. 1). The outer surface of the sample was held in the passive region at 400 mV (SCE). The recorded current decreased from an initially higher value to the passive value ($\gtrsim 0.03$ mA cm^{-2}) yielding a current transient that was similar to those obtained in the polarization curve measurements of the passive region. The cross section of the pit, after testing for 72 h, is shown in Fig. 4. No changes were found on the pit wall (100 times magnification), confirming that the whole pit remained in the pas-
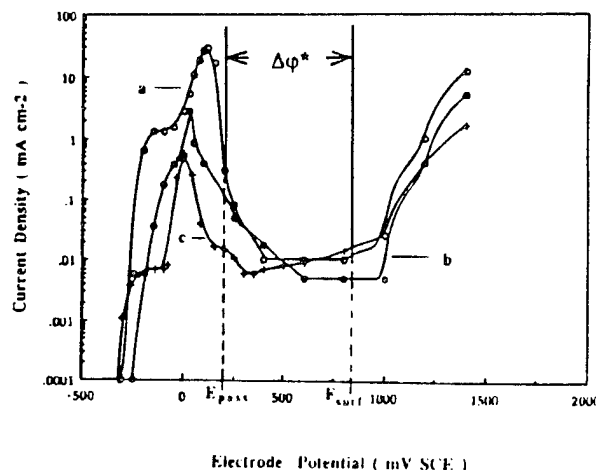

Fig. 3. Quasi-stationary polarization curves of Ni: in N_2 purged (a) $1N$ H_2SO_4, 800 ml with the surface facing either upward or sideway; (b) $1N H_2SO_4$ saturated with nickel sulfate, 200 ml with the surface facing upward; (c) 0.02 N H_2SO_4 saturated with NiSO$_4$, 200 ml with the surface facing upward.

Fig. 4. Cross section of an artificial pit in Ni after 72 h in 1 N H₂SO₄ showing no change in diameter (1 mm) or depth (5 mm). The sample's outer surface was held at 400 mV SCE with the pit opening faced downward.

sive state during the entire testing period. No pitting corrosion occurred for this pit.

However, when the initial pit depth was increased to 7 mm with the other conditions remaining the same, dramatic changes took place. Cross sections of artificial pits of approximately 7 mm depth (with their openings facing downward) at different times are presented in Fig. 5. The first pit, after 6 h of testing, had undergone a shape change. The cross section was noticeably larger (Fig. 5b). Proceeding into the pit from the bottom surface, one sees that for the first 1.4 mm (arrow), the pit remained at the original diameter. Further in, the pit was larger from aggressive nickel dissolution with the maximum diameter (peak current density) at about 1.8 mm. The dissolution rate was less (the diameter of the pit is smaller) at >1.8 mm, but still finite even at 7 mm (top of the micrograph). At longer times (Fig. 5c and e) this shape of the anodic current distribution is more pronounced and the active/passive boundary (identified by the arrow in Fig. 5b) moves toward the pit opening, gradually approaching the sample's outer (bottom) surface. Microscopic examination of the pit wall revealed a very rough, faceted condition at the early stages. With increasing test time (Fig. 5c-d) the morphology of the pit wall in the heavily dissolved (high current) region became less rough and less crystallographic in appearance; rather the pit wall became somewhat smooth in appearance. Smoothing during pit growth has been observed previously in iron and attributed to ferrous sulfate salt film formation on the pit surface.[11] Similar observations were made for the 10 mm deep pits.

Prior to the pit becoming inactive at 60 h (Fig. 5e), penetration of the outer (bottom) surface from inside the pit occurred, followed by passivation locally at the new opening. Then, another penetration of the surface occurred followed again by local passivation. This process was repeti-

tive, forming additional small holes around the original pit opening (arrows point to some of these penetrations in the cross section photograph of Fig. 5e) until growth of the pit ceased at 60 h. The sequential formation of holes moving outward from the original opening, has been reported in the literature.[3,11-15] The large number and arrangement of the holes has been described as a lace-like pattern. A typical photograph of the outer surface showing the new holes (arrows) around the original pit opening for another sample is presented in Fig. 6. The new holes again formed along a radial front moving outward from the center of the original pit opening. As the number of holes increased, the pitting process in Fig. 6 became less stable and eventually (at 110 h) ceased. This loss of stability of the pitting process with increasing number of penetrations was previously observed for stainless steel,[11,12] iron,[3,11,14] and Al bronze.[15] The lace-like morphology and the other results shown in Fig. 5 and 6 were also obtained for pits of different original depths (>7 mm). Microscopic examination (100 times) of the underside of the metal covering the pit revealed the same features reported above for the pit wall.

The above pitting corrosion tests were conducted with the pit opening facing downward. Experiments with the sample surface facing upward and the pit also open at the bottom (Fig. 2) produced a similar vase-like shape, but it was inverted from that shown in Fig. 5. When the sample surface was facing upward and had only the one opening at the top so that the corrosion products accumulated in the pit (right-side-up orientation), susceptibility to pitting was initially the same, *i.e.*, the initial pitting current was the same for pits with aspect ratios that satisfied the IR > Δφ* condition, but there was a major difference thereafter in that the pits facing upward prematurely went inactive. In subsequent cross-sectional examinations of these pits, some metal dissolution was evident and corrosion products were visible on the pit wall but the total amount of corrosion was small.

Potential distributions within the pit.—The measured potential distributions within the growing pits (original depth 7 mm in the upside-down orientation) are presented in Fig. 7. The local electrode potential decreases with increasing distance into the pit and even at the earliest recorded time (0.5 h) much of the pit wall is in the active region of the polarization curve (≳180 mV SCE from curve a in Fig. 3), in accord with the active dissolution noted beyond a certain distance in the cross sections of Fig. 5. The gradients near the pit opening are steeper at longer times but level off to approach the same potential deeper into the pit, about −30 mV (SCE). Thus, the location of a given potential, *e.g.*, $E_{pass} \approx 180$ mV (SCE), moves left in Fig. 7 toward the pit opening with increasing time. This shift in the potential distribution with time identifies a characteristic feature of the pit growth process: the active region of nickel dissolution expands toward the pit opening with time, in agreement with the photographic observations in Fig. 5. Sometime between measurement of the 40.5 h curve in Fig. 7 and cessation of pit growth at 60 h, the potential distribution reversed its trend and moved in the more noble direction. These data were not recorded for the sample in Fig. 5e but were for other samples during slow down of the growth of the pits. This reverse trend at late stages is schematically indicated by the dashed curve in Fig. 7 and shown by the measured curves in Fig. 8.

Typical potential distributions for a 10 mm deep pit in the right-side-up orientation (corrosion products accumulate in the pit) are shown in Fig. 8. The applied potential at its outer surface was also 400 mV (SCE). The earliest (0.5 h) measured potential distribution was similar to that presented for the upside-down orientation (Fig. 7), causing active dissolution of the pit wall. Thereafter, the potential profiles revealed the trend of a pit going inactive. The potentials moved in the more noble direction with increasing time, indicating that passivation of the pit was occurring at a very early time, less than a few hours compared to tens of hours for pits facing downward, *e.g.*, the pits in Fig. 5e and 6. This very early passivation for the right-side-up ori-
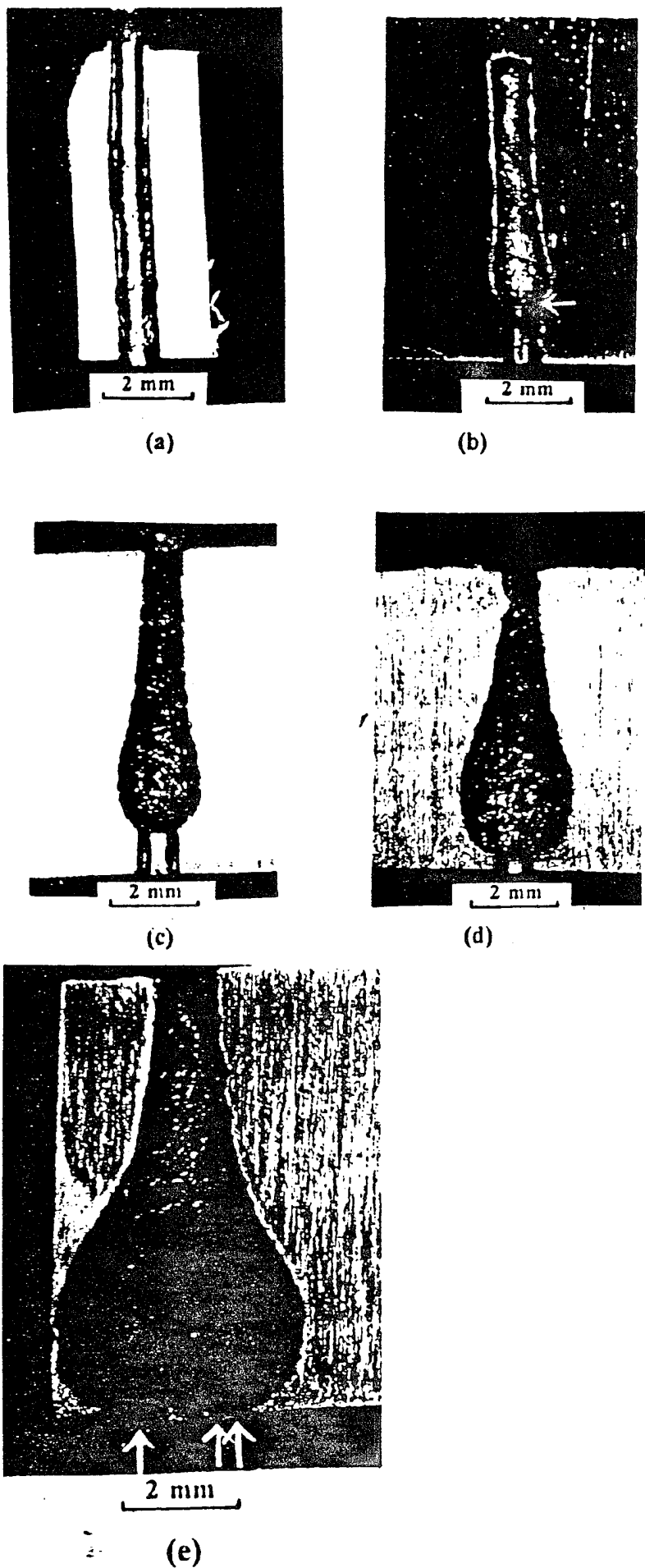
(a)

(b)

(c)

(d)

Fig. 5. Cross sections of a set of five artificial pits of 7 and 1 mm original depth and diameter, respectively. The outer surfaces were held at 400 mV (SCE) in $1N$ H_2SO_4, within the passive region of the polarization curve and the pit openings faced downward (a) 0 (original pit); (b) 6; (c) 24; (d) 44; (e) 60 h.

(e)

Fig. 6. Photograph of the outer surface of a sample tested for 110 h showing a lace-like pattern around the original pit opening, produced by multiple penetrations of the outer surface from inside the pit. Original depth: 10 mm; original diameter: 1 mm; outer surface potential: 400 mV SCE; pit opening faced downward.

Distance into the pit (mm)

Fig. 8. The measured potential distributions inside an artificial pit of original depth, 10 mm, and diameter, 1 mm, the opening of which faced upward resulting in accumulation of the corrosion products in the pit. Outer surface potential: 400 mV SCE.

entation occurs for a different reason than for the upside-down orientation since it occurs long before penetrations of the outer surface occur from inside the pit.

Another difference between the right-side-up and up-side-down orientations is the magnitude of the least noble potential measured in the pit, approximately −120 mV, SCE, for the right-side-up orientation (Fig. 8) compared to −30 mV, SCE, for the upside-down orientation (Fig. 7). Both of these least noble measured potentials are positive of the hydrogen evolution potential, consistent with the fact that (hydrogen) gas bubbles were never observed inside, or coming out of, the pits.

Current-time transient for the pit.—A typical current transient during an upside-down pit growth test is presented in Fig. 9a for the sample whose pit became inactive at 60 h (Fig. 5e). The transient for the sample in Fig. 6 is shown in Fig. 9b. The transient of Fig. 9c is for a sample with the pit opening facing upward (Fig. 8). The initial current for the pit facing downward (Fig. 9a) was about 2 mA and decreasing, typical of an initially active surface undergoing passivation. However, the current decreased to only about 1.5 mA prior to a gradual increase in current, indicating that some of the inside surface of the artificial
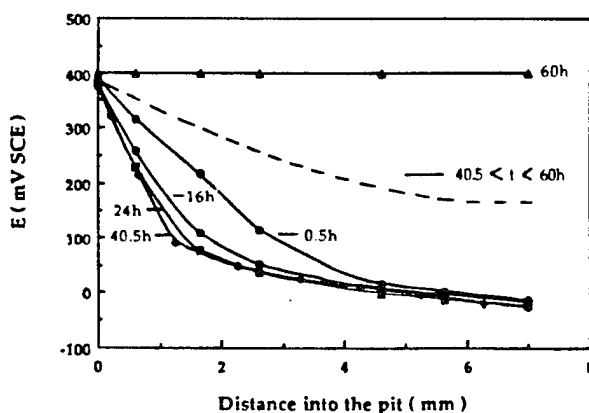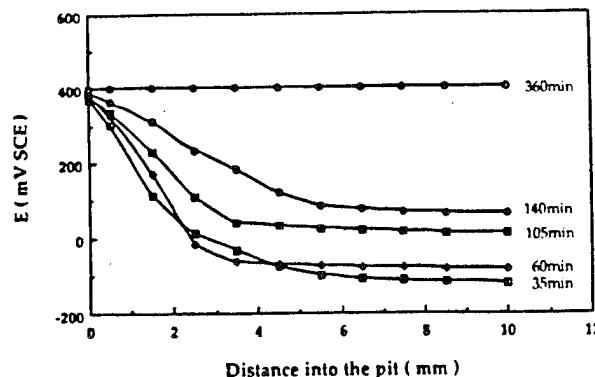

Distance into the pit (mm)

Fig. 7. The measured potential distributions in the artificial pit sample of Fig. 5e at different times.

pit remained in the active state. The current increased for hours until after many penetrations of the outer surface and then (at 60 h) the current abruptly decreased to zero and all pit growth activity ceased. The current transient of Fig. 9b, however, exhibits a current decrease but then a recovery in the period between 48 and 70 h. This slowdown of the pit growth rate, followed by recovery, occurred in the later stage when penetrations of the outer surface from within were occurring. Presumably, passivation of much of the pit surface momentarily occurred following one or more penetrations. This decrease-recovery pattern in the current was also observed in another sample during the lace-like pattern formation. Since the lace-like patterns differed from sample to sample, the later stages of the current transients were quantitatively different resulting in different times of active pitting and current values (e.g., Fig. 9a vs. 9b), though the qualitative trends were the same. The initial stages of the transients were more quantitatively reproducible.

For the samples with their pit opening facing upward (right-side-up orientation) so that the corrosion products accumulated within the pit promoting stagnation of the pit solution, the current transient has a markedly different trend (Fig. 9c). Initially, the current was large (2 mA) and of the same magnitude as the current of the samples facing downward (2 mA, Fig. 9a). This large initial pitting current was matched by a large potential gradient inside the pit (e.g., the earliest measured curve at 35 min, Fig. 8) that placed the potential inside the pit in the active region of the polarization curve (Fig. 3). However, the current declined instead of increasing with time. This coincided with a decrease in the potential gradient and the shift of the local electrode potentials in the pit to more noble values (35 to 140 min curves in Fig. 8) indicative of a slowdown in the growth of the pits after their brief initial high rate of growth. Thus, within hours potentials in the pit approached the outer surface potential of 400 mV (SCE). At this time, the entire pit wall became passivated; thus, the initial active state was not sustainable inside the pit and the pitting process was over in a matter of hours. Moving the Luggin probe into and out of the pit was found to increase the current, stimulating pit growth, and delaying the passivation process. In the case of Fig. 9c, a delay of over 3 h was produced by motion of the probe (compared to measured life times of 1 to 3 h for quiescent pit solutions).

Corrosion products in the pit and pH of the pit solution.—The nickel contents in the bulk solution and in the solution collected in the cylindroid of Fig. 2 after the pit growth test of an artificial pit (10 mm in depth and 1 mm in diameter with the outer surface held at 400 mV) for 93 h were analyzed. The nickel content in the bulk solution was 690 ppm. The nickel content in the solution of the cylindroid was much higher, 9850 ppm indicating that most of the Ni^{++} ion moved downward out of the pit by

convective flow of the denser pit solution under the influence of gravity.

The pH of the $1N$ H_2SO_4 bulk solution, which was the same as the pit solution at the beginning of the pitting process ($t = 0$), was measured using pH test paper and found to be 0.5 ± 0.2. During the pitting test for a pit (7 mm depth and 1 mm diam) facing downward (Fig. 5), some of the pit solution was extracted using a syringe and a fine pipette at $t = 6, 24$, and 44 h. Their pH at the three times was found to be 0.5 ± 0.2, indicating there was no change in the pH of the pit solution during the pit growth test. This same result was obtained in a second and third test. This constancy of the pH of the pit electrolyte is indicative of mixing of the bulk and pit solutions caused by the downward flow of the denser corrosion products out of the (upside-down) pit. If extensive mixing had not occurred, one would have expected, based on observations[16] and modeling results,[17] that the pH would rise somewhat in the pit solution to the equilibrium pH for the hydrolysis reaction. In another series of

Fig. 10. Comparison of the computed ($t = 0$) and measured (0.5 h) potential distributions ▬▬▬ for a pit of 7 mm in depth and 1 mm in diam, with the outer surface held at 400 mV (SCE) facing downward in $1N$ H_2SO_4.

tests using the right-side-up arrangement, the pH indeed was found to be approximately 2 at the end of the short (1 to 3 h) lifetimes of the pits. This increase in pH is consistent with the fact that convective mixing of the pit and bulk solutions is much less for the right-side-up orientation.

Calculated potential and current distributions.—The initial potential and dissolution current distributions within pits of the same diameter, 1 mm, and different depths were calculated using the computation method published earlier.[6,7] The polarization data of curve a in Fig. 3 were used in the computation. A comparison between one computed potential distribution for a pit depth of 7 mm and the experimental result at 0.5 h is presented in Fig. 10. The computed potential profiles in Fig. 11 for the 7 and 50 mm deep pits are very steep (indicative of large potential drops within the pits) and are similar to the measured profiles for the 7 mm deep artificial pits (Fig. 7 and 10). In contrast, the computed potential profile for the 3.5 mm deep pit (Fig. 11) is almost horizontal (very small potential drop within the pit), indicating that no pitting occurs for a 3.5 mm deep artificial pit. Similarly, the measured potential profile of the 5 mm deep pit in Fig. 4 for which there was no corrosive attack, was also almost horizontal. Thus the modeling correctly predicts that the artificial pits of 7 mm depth will undergo anodic dissolution, while a shallower pit (3.5 mm) will not. The computational result that the 3.5 mm deep pit is completely passive is not inconsistent with the observation that the active/passive boundary in the experimental results of Fig. 5 is at less than 2 mm for two reasons. The E_{pass} value moves toward the pit
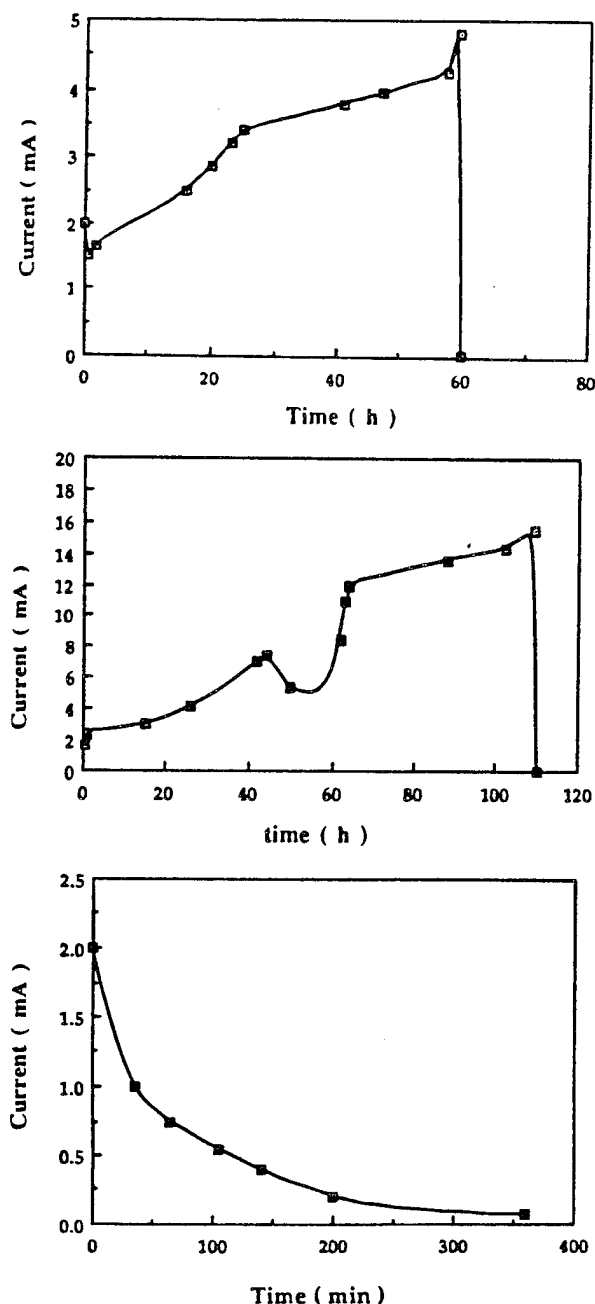

Fig. 9. Pitting current transients during the pit growth test: (a) for the sample of Fig. 5e; (b) for the sample of Fig. 6; (c) for the sample with the pit opening facing upward (Fig. 8).
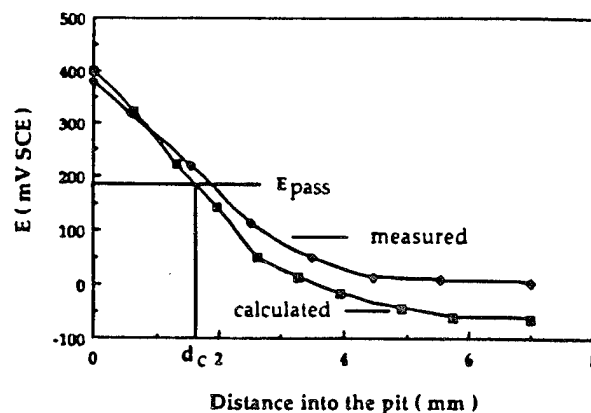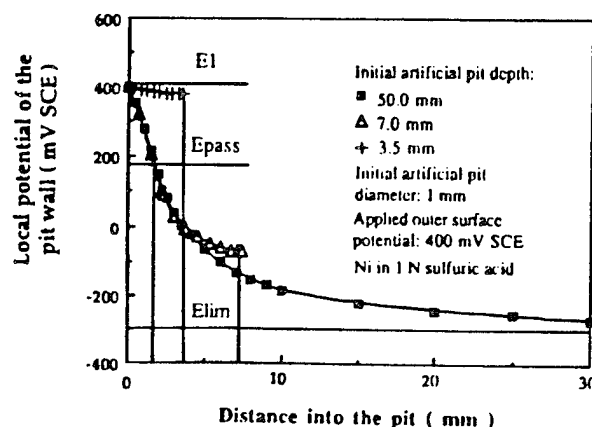

Fig. 11. Computed initial potential distributions within pits in the nickel/$1N$ H_2SO_4 system. The pits are 3.5, 7.0 and 50 mm in depth and 1 mm in diam, with the sample's outer surface held at 400 mV (SCE) in the passive state.
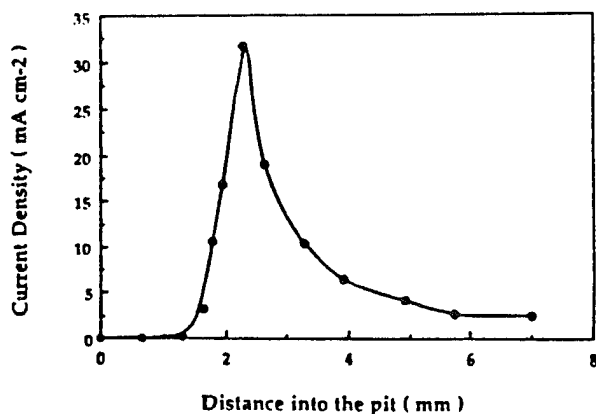
Fig. 12. Computed initial pitting current distribution on the pit wall (corresponding to the pit of 7 mm depth in Fig. 11).

opening with increasing time (Fig. 5). Hence, it is at its greatest distance from the pit opening at $t = 0$ rather than at $t > 0$ as in Fig. 5. Second, the location of E_{pass} on the pit wall at $t = 0$ (critical distance, d_c) is a function of the original pit depth (d_o); d_c increases as d_o decreases.[7]

The corresponding computed current distribution on the artificial pit wall for the 7 mm deep pit is presented in Fig. 12. It shows a large current peak just beyond the distance of the passive to active transition on the pit wall. Thus, the modeling also yields a current distribution similar to that observed (Fig. 5).

Discussion

Voltage drop mechanism of pit growth.—Previous work[1-7,17] suggests that localized corrosion is due to a macrocorrosion cell where the anode site within the cavity has electrode potentials within the active region of the polarization curve of the cavity electrolyte which is at less noble potentials than the outer surface cathodic site. The outer surface is at a potential in the passive region that is maintained by either a potentiostat in a laboratory test or an oxidant (*e.g.*, oxygen) in the natural environment. The potential distribution within a crevice or a pit is decided by: (*i*) the electrodynamics described by the time dependent diffusion-migration equation. In ideal/simplified cases, the time independent Poisson or even Laplace equation may be used. (*ii*) The polarization and passivation effects which promote the penetration of the applied electric field into the crevice or pit. (*iii*) The IR, which results from the flow of the corrosion current, balances the electrode potential difference between the anode in the cavity and the cathode outside the cavity.

In simple cases (an active loop exists in the bulk solution polarization curve enabling immediate commencement of the pit growth process for aspect ratios that satisfy the IR > $\Delta\phi^*$ condition[1-7]) the initial potential distribution may be calculated quantitatively.[6,7] Both experimental and computational results show that when the depth of a pit is small relative to its diameter (or the depth of a crevice is small relative to its gap dimension), *i.e.*, the aspect ratio is small, the current decreases as the pit or crevice walls become fully passivated due to the influence of the applied electric field. Hence, no localized corrosion occurs. When the cavity depth is greater (exceeding the critical depth for a given pit diameter or gap dimension[6,7]), the IR condition for stable localized corrosion is met at $t = 0$, *i.e.*, the IR drop, IR = $E_{surf} - E_{pit}$ (or $E_{crevice}$) > $\Delta\phi^*$ (Fig. 3), will exist in the cavity electrolyte between the anode (the active pit or crevice wall) and the outer surface.

The voltage drop mechanism is able to explain, qualitatively and to some extent quantitatively, many of the established facts for pitting (or crevice) corrosion. For example, the observed very large pitting corrosion rate may be explained by the different local electrode potentials of the anode (the pit or crevice wall) which yields a very large anodic dissolution current density (could be as large as the

peak current in the polarization curve). The latter can be a thousand times larger than the metal dissolution rate at the outer surface which is at a more noble potential in the passive region. The roles of the chloride ion and of local acidification and the manner in which the initial stabilization of the pitting or crevice corrosion process occurs, can also be explained within the framework of the voltage drop mechanism.[1-7] In the following sections, the validity of the voltage drop mechanism is further examined by the experimental/modeling results of the present work.

Morphology change of the artificial pit during growth.—The shape evolution of the cross section of the corroding pits (Fig. 5) is very similar to the shape evolution observed in artificial pits for iron in acetic acid.[7] The vase shape is due to the initial cylindrical geometry of the artificial pit and to the current distribution dictated by the shape of the active peak of the polarization curve of the pit electrolyte, *i.e.*, the highest pitting current density ($\equiv$ the peak current density of the polarization curve) is just slightly deeper into the pit than the active/passive boundary on the pit wall, and the current density decreases at greater distances into the pit. With the accompanying increase in diameter of the active part of the pit, the dissolution area increases. Thus, the total pitting current increases with time (Fig. 9a and b). As a result, a shorter current flow path can produce the required IR drop to maintain a portion of the pit wall in the active state; hence the active/passive boundary on the pit wall is expected to move toward the pit opening with increasing time, consistent with the experiments (Fig. 5 and 7). Accordingly, the pit expands also in the direction of the outer surface with increasing time, and eventually penetrates the outer surface from underneath (Fig. 5e and 6). The penetration produces a new pit opening which causes the IR drop to suddenly decrease owing to the new electrolyte path between the pit and bulk solutions so that the stability condition IR > $\Delta\phi^*$ may no longer be met anywhere in the pit. Hence, the entire pit surface may passivate leaving an inactive pit of approximately hemispherical shape.

Lace-like morphology of the external surface.—When a penetration of the external surface occurs, typically, the local region of the penetration passivates while the remaining pit wall further from the new hole still remains in the active state. Two explanations of the passivation of the pit wall in the vicinity of the new opening have been offered in the literature: (*i*) dilution of the pit solution, in particular the H^+ and Cl^- ion concentrations, by entry of bulk electrolyte[11] and (*ii*) decrease in the IR drop as a result of the new electrolyte path for current flow.[3] The latter IR drop mechanism can explain all of the known features of the lace-like morphology, *e.g.*, the rough, faceted nature of the pit wall including near the new openings as reported above and elsewhere,[11,14] is readily explained by the local electrode potential being in the Tafel region of the active peak, prior to formation of the new hole.[3] The presence of salt films on the pit surface[11] is also indicative of potentials in the active peak. The tendency to form new holes in a concentric pattern around the original pit opening and then in a larger concentric pattern, and so on, is expected behavior for the IR mechanism.[3] Furthermore, it has been experimentally found in this work and earlier studies[3,7] that the IR drop controls the motion of the active/passive boundary toward the pit opening and that this motion is a precursor step to the formation of the new holes that produce the lace-like morphology. Hence, the results indicate that prior to formation of the new hole, the underneath surface of the metal covering the pit is at a less positive potential (in the active region) than that of the outer surface which is in the passive region. It follows that when a penetration occurs, the existing IR drop is short circuited through the new hole. This causes the local electrode potential on the pit wall at this hole to shift in the positive direction approaching the outer surface potential. Consequently, the pit wall at the new hole passivates, precluding further enlargement of the opening.[3]

That the IR drop is the basis of the lace-like pitted structures is also indicated from a consideration of the time constants of the IR short-circuiting and diffuse mixing processes. When the new hole forms, short-circuiting of the IR drop occurs in a matter of seconds whereas diffusive mixing of the pit and bulk volumes takes much longer. For example, under quiescent conditions it takes on the order of 1 h for species with diffusivities of 10^{-5} cm^2 s^{-1} to traverse 1 mm (root mean square displacement equation). If the time constant for diffusive mixing was shorter, *e.g.*, seconds or minutes, the pits that went inactive in one or a few hours under stagnant conditions (*e.g.*, Fig. 8 and 9c) would have remained active since the mixing rate would then be much faster than the time constant for saturation of the pit solution in NiSO$_4$. The latter saturation time constant can be easily shown from the charge passed (*e.g.*, area under curve c in Fig. 9) and the volume of the artificial pit to be also on the order of hours.

The roles of the corrosion products, pH, and resistivity.— The results of Fig. 5-7, 9a and b, and 10 were obtained from samples with their pit opening facing downward, while the results of Fig. 8 and 9c were from a sample with its pit facing upward. The large difference between these two sets of results is related to the more stagnant solution inside the pits with the right-side-up orientation. The reason that stagnancy decreases the pit stability in this metal/electrolyte system is indicated in the polarization curves of Fig. 3. The peak current density in the active region for the two solutions saturated with nickel sulfate (curves b and c) is substantially lower and located at less noble potentials than that for the solution without nickel sulfate. The peak current density of curve c is lower than that of curve b (curve c is for the higher pH solution). A smaller active peak that is at less noble potentials makes it more difficult to maintain the stability criterion: IR > $\Delta\phi^*$, since the current produced in the active region of the pit wall, I, is smaller and $\Delta\phi^*$ is larger[1,3-5]; the higher (measured) resistivity of these saturated solutions (R is increased) tends to compensate for the decreased size of the active peak but the fourfold increase in R is not dominant considering that the current decreases by one to two orders of magnitude. The dominancy of the decrease in size of the active peak is borne out by the fact that the pits in the right-side-up orientation become less active with increasing time (Fig. 8 and 9c). This explanation of how the change in solution composition of a stagnant pit solution with increasing time causes a destabilization of the pitting process for the right-side-up orientation is also supported by the observation that motion of the Luggin probe in and out of the pit, effectively diluting the pit solution with bulk solution, extends the pit life (Fig. 8 and 9c). In an earlier experiment with iron in a pH 3.9 solution, the pitting process was also found to be stimulated by the motion of the probe: matching current and potential spikes were simultaneously initiated upon insertion of the probe into the pit.[17] In this case motion of the probe disturbed the hydrogen gas bubble which filled the bottom portion of the pit and resulted in the sharp current/potential fluctuations since the gas/pit-wall spacing determined the resistance to current flow.[17]

For pits facing downward (*e.g.*, Fig. 5), however, the situation is different in that the size of the active peak for the pit electrolyte remains near that of the starting bulk solution (Fig. 3, curve a) as shown above by the measured constancy of pH during the experiment. The more dense NiSO$_4$ solution easily moves downward out of the pit in the direction of gravity, effectively maintaining a dilute Ni^{2+} concentration and the bulk solution pH and resistivity in the pit. Accordingly, since both IR and $\Delta\phi^*$ retain their initial values, the IR > $\Delta\phi^*$ condition which initiated the pitting process is maintained for the up-side-down orientation and a stable pitting process ensues. Consequently, only after penetrations of the outer surface occur does destabilization of the pitting process commence. (Note that stable pit growth probably would not have occurred in the first place had an oxidant instead of the potentiostat been used since the oxi-

dant would not have become depleted in the artificial pit in view of the strong convective mixing.)

The onset of active metal dissolution in the artificial pit may be independent of the pit orientation (facing up *vs.* down) since the Ni^{2+} ion content, pH, conductivity, and the IR > $\Delta\phi^*$ condition are initially the same in the pit for both orientations. The same initial pitting current of Fig. 9a and c (~2 mA) supports this statement.

The above mentioned increase in pH from 0.5 to 2 for the stagnant solution (right-side-up orientation) occurs under the influence of the potential gradient existing in the pit solution.[17] The onset of the hydrolysis reaction keeps the pH from rising more. Thus, in bulk solutions whose pH is lower than the hydrolysis equilibrium pH (in which case the hydrolysis reaction does not occur), the pH increases in a stagnant solution with increasing time to a new stable value and, along with the increase in metal ion concentration, causes the above mentioned decrease in size of the active peak (Fig. 3). For the Ni/1N H$_2$SO$_4$ system this means that a less favorable IR > $\Delta\phi^*$ condition develops during the pitting process so that destabilization of the pitting process occurs (Fig. 8 and 9c).

The pH change has the opposite effect when the bulk solution pH is greater than the equilibrium pH of the hydrolysis reaction, *e.g.*, in neutral and alkaline solutions. The pH now decreases in a stagnant solution (right-side-up orientation) because of the occurrence of the hydrolysis reaction.[16] Since the metal ion concentration increases in the pit regardless of the pH, these two factors that mainly determine the size of the active peak, metal ion concentration and pH, oppose each other. It follows that if the decrease in pH dominates, the size of the active peak increases for the stagnant solution inside a pit. This makes the IR > $\Delta\phi^*$ condition more easily met as the pit solution stagnates with increasing time, and visa versa if the metal ion concentration dominates.

The resistivity change in neutral or alkaline solutions can also have the opposite effect to that in strongly acid solution. Since the hydrolysis reaction occurs (neutral and alkaline solutions) and increases the concentration of the very mobile H$^+$ ion, the conductivity of a stagnant pit solution (right-side-up orientation) can be expected to increase during the experiment, *i.e.*, R decreases with increasing time to a new stable value. Thus, if the active peak also becomes smaller (which would happen if the increase in metal ion concentration dominates over that of the H$^+$ ion as discussed above), the IR > $\Delta\phi^*$ condition becomes more difficult to meet as the pit solution stagnates. If, on the other hand, the active peak increases in size (the increase in H$^+$ ion concentration dominates over the increase in metal ion concentration) and is dominant over the resistivity decrease, IR > $\Delta\phi^*$ would become easier to meet during the stagnation process. This latter situation is thought to be the explanation for the delayed onset of crevice corrosion observed in laboratory and service exposures in neutral and alkaline environments. This anticipated dominance of the increase in size of the active peak over the decrease in resistivity is reasonable since it was found above to occur in the case of the strongly acid solutions. Accordingly, the right-side-up orientation with its inherent tendency for stagnation of the solution would more readily produce stable localized corrosion than the upside-down orientation in the case of neutral and alkaline bulk solutions.

The computational results in Fig. 11 which are for curve a in Fig. 3 (1N H$_2$SO$_4$) show that the outer surface polarization extends to over 30 mm into the pit. The potential is still decreasing at this distance in the approach to the limiting potential. E_{lim} is established by the mixed potential of the nickel dissolution reaction and the hydrogen evolution reaction and exists at depths beyond the reach of the outer surface polarization.[1] For nickel in 1N H$_2$SO$_4$ saturated in Ni^{2+} ion, E_{lim} can be expected to be close to the above reported corrosion potential for the deaerated 1N H$_2$SO$_4$ solution, *i.e.*, $E_{lim} \cong -300$ mV (SCE). This is considerably more negative than the -30 mV (SCE) value measured for the 7 mm deep pit (Fig. 7). Since for the up-side-down

orientation good mixing occurs so that curve a in Fig. 3 (and the bulk solution conductivity) approximately applies at $t > 0$, one reason that E_{lim} is not reached in the above experiments (e.g., Fig. 7) is that the outer surface polarization extends to the bottom of the 7 and 10 mm deep pits (Fig. 11). The least noble measured potential was -120 mV (SCE) in Fig. 8 (35 min curve) for this unstable pit growth situation (stagnant solution, right-side-up orientation). This more negative measured potential (compared to the -30 mV SCE for the upside-down orientation in Fig. 7) is in accord with the measured lower conductivity for the more saturated, higher pH solution (for otherwise roughly the same current at 0.5 h) and with this pit's longer current path (10 mm depth), i.e., R is larger for the pit in Fig. 8 that gave the larger IR drop.

The existence of a salt film could explain the origin of the plateau (shoulder) that exists in the active peaks of the polarization curves (Fig. 3). A salt film could also produce the smoothing of the faceted pit walls reported above at later stages of pit growth. This interpretation is consistent with the fact that the most negative measured potential during stable pitting, -30 mV, SCE (upside down orientation, Fig. 7) lies near the positive end of the plateau in curve a of Fig. 3. If a salt film does form it could support a significant IR drop. This IR drop, however, would not be detected by the measuring technique[3] or by the calculation used in this paper. Its magnitude could be as large as the difference between the least noble measured potential in the pit and the limiting potential. A finite resistance of the salt film to current flow would mean that the actual current flowing through the pit electrolyte would be less than at earlier times when a salt film had not yet formed. Thus, the measured potential profile at early times (e.g., 0.5 h) could be at less noble potentials than the calculated profile, e.g., as in Fig. 10, since the calculated profile used the polarization curve a in Fig. 3 which contains the current plateau in the active region that may be the result of a salt film.

Quantitative evidence of the voltage drop mechanism.— In this study, the IR-based model successfully predicted the depth of 1 mm diam pits that would be susceptible to the onset of pitting. Other quantitative comparisons of the IR model and the experimental results are developed and presented in this section.

Location of the active/passive transition.—The location of the active/passive boundary on the crevice wall as a function of time may be determined visually from the photographs of the cross section of the pit (Fig. 5). It is at $x = 1.4$ mm at 6 h (Fig. 5b, arrow) and at smaller x values at longer times. From this 6 h photograph it can be deduced to have been near $x \cong 1.8$ mm at some earlier time since the pit diameter increases gradually beyond 1.4 mm, reaching a maximum at $x = 1.8$ mm. The value at $t = 0$, however, cannot be determined from examination of Fig. 5. This boundary location can also be roughly estimated from the following equation and the available data

$$d_c = \frac{I - \sqrt{I^2 - 0.5\pi^2 \sigma D^3 i_{pass} \Delta\phi^*}}{\pi D i_{pass}} \qquad [1]$$

Derivation of Eq. 1 is similar to that given in the Appendix of Ref. 6 for the analogous case of a crevice. It contains only parameters that are directly available from the experimental data, i.e., the pitting current, $I = 1.8$ mA (Fig. 9a, average current between $t = 0$ to 1 h); the conductivity for $1N$ sulfuric acid, $\sigma = 0.195$ Ω^{-1} cm^{-1} (measured value); the diameter of the pit, $D \cong 1$ mm between $t = 0$ to 1 h; the passive current density (Fig. 3), the average value of $i_{pass} \cong 0.02$ mA cm^{-2}; and the potential difference between the applied passive potential at the sample's outer surface ($E_{surf} = 400$ mV, SCE) and the active/passive transition potential ($E_{pass} \cong 180$ mV, SCE, from Fig. 3, curve a), $\Delta\phi^* = 220$ mV. The critical distance at an early time from Eq. 1 is $d_c \cong 1.9$ mm. This value is of the same order of magnitude as the estimated value from the data in Fig. 5 discussed above (~ 1.8 mm) which is all one can expect without knowing the experimental values at $t = 0$. This good agreement is a proof of the IR voltage drop mechanism.

Potential distribution within a pit.—The comparison between the computed[6] and the measured potential distribution for a pit of depth 7 mm and diameter 1 mm is shown in Fig. 10. The two curves are very close to each other except at the pit opening and near the bottom of the pit where the measured potentials differ from the computation to some extent. The calculation is for conditions at $t = 0$ when the diameter of the artificial pit is 1 mm; the active peak is assumed to be that given by curve a in Fig. 3 although this curve is at $t > 0$ when a salt film may have existed on the sample surface. The earliest measured potential distribution is at 0.5 h by which time the pit geometry is more complicated than the $t = 0$ geometry. The size of the active peak and electrolyte resistivity, however, should be close to the $t = 0$ values, since for the data in Fig. 10 good mixing of the pit and bulk solutions occurred by virtue of the upside-down orientation. These and other sources of error are discussed next.

At the pit opening ($x < 1$ mm), the measured potential does not decrease with the pit depth as steeply as the computation predicts. This is believed to be due to the "pit opening effect," explained as follows. Referring to Fig. 13a, point A is inside the pit far away from the pit opening. The measured potential at A is actually the average potential of the small area (Δx) around A which is "sensed" by the tip of the Luggin probe. Since the "sensed area," Δx, is very small, the potential distribution in this area can be considered linear. Thus, the average potential (the measured potential) is the potential at the middle point of Δx, point A. At point B close to the pit opening, however, the situation is quite different. The "sensed area," $\Delta x'$, extends out of the pit where the electrode potential changes little since the resistance to current flow is much less. The average potential (the measured potential) is thus the lower potential at
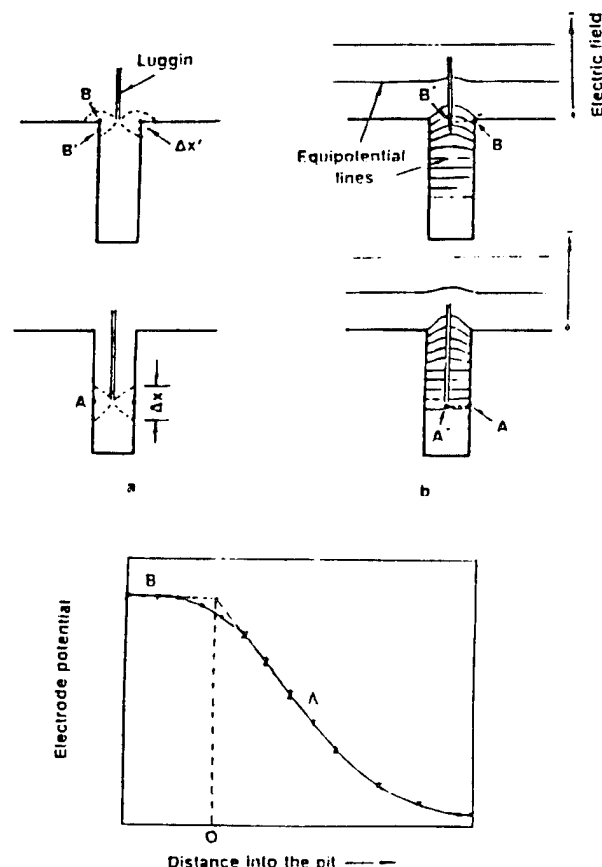

Fig. 13. Schematic descriptions of the "pit opening effect" in the potential measurements. (a) The effect of the "sensed area" by the Luggin probe. (b) The effect of the convex equipotential lines at the pit opening. (c) Determination of the pit opening location.

B', close to the bottom part of $\Delta x'$, instead of the potential at B. Another reason for the pit opening effect is the convex shape of the equipotential lines in the pit opening area, as shown in Fig. 13b. At point A away from the pit opening, the equipotential line is nearly horizontal. Thus, the potential at A*, the tip of the Luggin probe, is equal to the potential at A. In the pit opening area, the equipotential lines are of convex shape. The potential at the tip of the Luggin probe, B*, is higher than that at B. The measured electrode potential is thus lower than the actual value at B by the amount $\Delta\phi = \phi_{B^*} - \phi_B$.

Due to the pit opening effect, the measured potential distribution is like the solid line in Fig. 13c. This measured distribution makes the pit opening position $x = 0$ difficult to determine accurately. However, the measured curve may be divided into two parts. Part A is the potential distribution inside the pit, in which the electrode potential drops rapidly with increasing distance into the pit. Part B is the potential outside the pit, in which the potential changes very little. Extrapolation of both Part A and Part B gives an intercept. This intercept, point O, is the pit opening point $x = 0$. All the measured curves in Fig. 7, 8, and 10 were drawn in this manner.

The difference in the calculated and measured curves in Fig. 10 in the bottom part of the pit could arise from: (*i*) the shape difference of the pit bottom. The bottom 2 to 3 mm of the pit in the experiment has the (cone) shape of the drill bit but the computation is based on a flat pit bottom. (*ii*) The change of the pit diameter and of the solution composition and conductivity. The measured potential distribution was at $t = 0.5$ h while the computation was based on the $t = 0$ parameters. The pit diameter increased somewhat in this 0.5 h period due to active dissolution of the pit wall; the change in solution composition and conductivity can be assumed to have been negligible for this upside-down orientation. (*iii*) Errors in the computation, *e.g.*, caused by idealized assumptions and in the measurement. The computation assumed that the initial conditions in the pit were represented by the quasi-stationary curve a in Fig. 3 whereas the currents may have initially been higher. Thus, although there is some difference, the two curves in Fig. 10 can be considered in quite good agreement with each other. This good agreement suggests that the assumptions for the computation are basically correct, which was already indicated in earlier comparisons of the calculated and experimental results.[6,7]

From the computed potential distributions for pits of 7 mm depth (Fig. 10 and 11), the critical distance is the value at the passivation potential, $E_{pass} \approx 180$ mV; $d_c \approx 1.7$ mm. This is in agreement with the estimated experimental value from Fig. 5 given above (~1.8 mm at 6 h > t > 0) and also with the above estimated value from Eq. 1, $d_c = 1.9$ mm.

Total pitting current in the early pitting stage.— Figure 12 shows the initial current distribution within the pit which was calculated for the 7 mm deep pit in Fig. 11 using the computation model.[6] The total pitting current may be obtained by integration of the curve over the pit wall

$$I = \int_0^{d_o} \pi D i \, dx \approx 1.8 \text{ mA}$$

where d_o is the pit depth. The obtained value is well within the range of the experimental data, 1.5 to 2 mA (Fig. 9a, $t = 0$ to 1 h). Thus, it can be concluded that the measured current largely reflects the rate of metal dissolution in the pit rather than being unduly influenced by oxygen reduction or some other reaction. A comparison of the charges passed from the current-time result and from the volume of metal dissolved (*e.g.*, Fig. 9a and Fig. 5e) also supports this conclusion.

All the above estimation and computation results are based on the voltage drop mechanism. The quantitative/semi-quantitative agreements between the computation and the experiment prove that the IR mechanism is operating for pitting corrosion in the Ni/1N H$_2$SO$_4$ system.

Conclusions

1. The growth of artificial pits in Ni in 1N H$_2$SO$_4$ occurs by the voltage drop mechanism.

2. The evolution of the pit shape, potential and current distributions on the pit wall, and formation of the lace-like morphology for the Ni/H$_2$SO$_4$ system have been explained in terms of the IR drop mechanism that was previously found to explain similar results for the iron/acetic acid (pH 4.7) system.[1-7]

3. The accumulation of Ni$^{\cdot\cdot}$ ions and increase in pH that occurs for stagnant conditions (right-side-up orientation) destabilizes the pitting corrosion process, and decreases the size of the active loop of the polarization curve in accord with the IR > $\Delta\phi^*$ criterion.

4. A mathematical model based on the Laplace equation and the anodic polarization curve successfully predicts susceptibility to the onset of pitting corrosion in artificial pits for the Ni/sulfuric acid system.

REFERENCES

1. H. W. Pickering, *Corros. Sci.*, **29**, 325 (1989); *Corrosion*, **42**, 25 (1986).
2. E. A. Nystrom, J. B. Lee, A. A. Sagüés, and H. W. Pickering, *This Journal*, **141**, 358 (1994).
3. A. Valdes, Ph.D. Thesis, The Pennyslvania State University, University Park (1987); A. Valdes and H. W. Pickering, in *Advances in Localized Corrosion*, NACE-9, H. Isaacs, U. Bertocci, J. Kruger, and Z. Szklarska-Smialowska, Editors, p. 393, NACE Houston, TX (1990).
4. K. Cho and H. W. Pickering, *This Journal*, **137**, 3313 (1990); *ibid.*, **138**, L56 (1991).
5. H. W. Pickering, K. Cho, and E. Nystrom, *Corros. Sci.*, **35**, 775 (1993).
6. Y. Xu and H. W. Pickering, *This Journal*, **140**, 658 (1993).
7. Y. Xu, M. Wang, and H. W. Pickering, *ibid.*, **140**, 3448 (1993).
8. J. C. Walton, *Corros. Sci.*, **30**, 915 (1990).
9. B. G. Ateya and H. W. Pickering, *This Journal*, **122**, 1018 (1975).
10. G. Trabanelli, F. Zucchi, and L. Felloni, *Corros. Sci.*, **9**, 673 (1969).
11. R. P. Frankenthal and H. W. Pickering, *This Journal*, **119**, 1304 (1972).
12. M. A. Streicher, *ibid.*, **103**, 375 (1956).
13. I. L. Rosenfeld and I. S. Danilow, *Z. Physik. Chem.*, **226**, 257 (1964).
14. M. G. Alvarez and J. R. Galvele, *Corros. Sci.*, **24**, 27 (1984).
15. B. G. Ateya, E. A. Ashour, and S. M. Sayed, *This Journal*, **141**, 71 (1994).
16. B. F. Brown, C. T. Fugii, and E. P. Dahlberg, *ibid.*, **116**, 218 (1969); J. A. Smith, M. H. Peterson, and B. F. Brown, *Corrosion*, **26**, 539 (1970).
17. H. W. Pickering and R. P. Frankenthal, *ibid.*, **119**, 1297 (1972).

DISTRIBUTION LIST

Dr. A. John Sedriks   3
Materials Division, Code 1131M
Office of Naval Research
800 N. Quincy Street
Arlington, VA 22217-5660

Mr. Gerald Smith   1
Office of Naval Research
Federal Building - 2nd Floor
536 S. Clark Street
Chicago, IL 60603-1588

BASIC DISTRIBUTION LIST

Technical Reports and Publications

Organization	Copies	Organization	Copies
Defense Technical Information Center Cameron Station Alexandria, VA 22304-6145	2	Naval Air Warfare Center Aircraft Division, Trenton Trenton, NJ 08628 ATTN: Library	1
Office of Naval Research 800 N. Quincy Street Arlington, VA 22217-5660 ATTN: Code 3310	3	Naval Facilities Engineering Service Center Port Hueneme, CA 94043 ATTN: Materials Div.	1

Naval Research Laboratory
4555 Overlook Ave, S.W.
Washington, DC 20375
ATTN: Code 6000
        Code 6300
        Code 5227
	1
	1
	1
		Naval Surface Warfare Center
		Carderock Division
		Bethesda, MD 20084
		ATTN: Library
			1

Naval Air Warfare Center White Oak Detachment Silver Spring, MD 20903-5000 ATTN: Library Code R33	1 1	Naval Underwater Warfare Ctr. Newport, RI 02840 ATTN: Library	1
Naval Postgraduate School Monterey, CA 93940 ATTN: Mechanical Engineering Department	1	Naval Air Warfare Center Weapons Division China Lake, CA 93555-6001 ATTN: Library	1
Naval Air Systems Command Washington, DC 20361 ATTN: Code 5304	1	NASA Lewis Research Center 21000 Brookpark Road Cleveland, OH 44135 ATTN: Library	1

Naval Sea Systems Command
Washington, DC 20362
ATTN: Code 05M
        Code 05R
	1
	1
		National Institute of
		Standards and Technology
		Gaithersburg, MD 20899
		ATTN: Metallurgy Division
		        Ceramics Division
		        Fracture & Deformation
		          Division
			1
			1
			
			1

Organization	Copies	Organization	Copies

Naval Command, Control and
Ocean Surveillance Center
R&D Division
San Diego, CA 92152-5000
ATTN: Library   1

Office of the Assistant Commander
HQ Marine Corps
2 Navy Annex
Washington, DC 20380-1775
ATTN: Scientific Advisor   1

Army Research Office
P.O. Box 12211
Research Triangle Park, NC 27709
ATTN: Metallurgy & Ceramics
         Program   1

Army Materials Technology
Laboratory
Watertown, MA 02172-0001
ATTN: SLCMT-TMM   1

Air Force Office of Scientific
Research
Building 410
Bolling Air Force Base
Washington, DC 20332
ATTN: Electronics & Materials
         Science Directorate 1

NASA Headquarters
Washington, DC 20546
ATTN: Code RN   1

Naval Surface Warfare Center
Port Hueneme Division
4363 Missile Way
Port Hueneme
CA 93043-4307
ATTN: Library   1

Metals Information Analysis Center
Purdue University
2595 Yeager Road
West Lafayette
IN 47906   1

Naval Facilities Engineering
Command
Alexandria, VA 22331
ATTN: Code 03   1

Oak Ridge National Laboratory
Metals and Ceramics Div.
P.O. Box X
Oak Ridge, TN 37380   1

Los Alamos Scientific Lab.
P.O. Box 1663
Los Alamos, NM 87544
ATTN: Report Librarian   1

Argonne National Laboratory
Metallurgy Division
P.O. Box 229
Lemont, IL 60439   1

Brookhaven National Laboratory
Upton, Long Island
NY 11973
ATTN: Research Library   1

Lawrence Berkeley Lab.
1 Cyclotron Rd
Berkeley, CA 94720
ATTN: Library   1

Naval Surface Warfare Center
Annapolis Detachment
Annapolis, MD 21402-5067
ATTN: Code 61   1
         Code 613   1
         Code 0115   1

Supplemental Distribution List

Profs. G.H. Meier and F.S.Pettit
Dept. of Mat'ls Science & Eng.
848 Benedum Hall
University of Pittsburgh
Pittsburgh, PA 15261

Prof. Gordon P. Bierwagen
North Dakota State University
Dept. of Polymers and Coatings
Box 5227
Fargo, ND 58105

Prof. H.W. Pickering
The Pennsylvania State Univ.
209 Steidle Bldg.
University Park, PA 16802

Prof. D.J. Duquette
Dept. of Metallurgical Eng.
Rensselaer Polytechnic Inst.
Troy, NY 12181

Prof. D. Tomanek
Michigan State University
Dept. of Physics and Astronomy
East Lansing, MI 48824-1116

Dr. M. W. Kendig
Rockwell International Sci.Ctr.
1049 Camino Dos Rios
P.O. Box 1085
Thousand Oaks, CA 91360

Prof. R. A. Rapp
Dept. of Metallurgical Eng.
The Ohio State University
116 West 19th Avenue
Columbus, OH 43210-1179

Dr. R.D. Granata
Sinclair Laboratory #7
Lehigh University
Bethleham, PA 18015

Dr. G. D. Davis
Martin Marietta Laboratories 848
1450 South Rolling Rd.
Baltimore, MD 21227-3898

Dr. S.M. Lipka
Dept. of Ocean Engineering
Florida Atlantic University
Boca Raton, FL 33431-0991

Dr. D.D. Macdonald
The Pennsylvania State Univ.
517 Deike Bldg.
University Park, PA 16802

Dr. B.G. Pound
SRI International
333 Ravenswood Ave.
Menlo Park, CA 94025

Prof. C.R. Clayton
Dept. of Materials Science & Eng.
State University of New York
Stony Brook
Long Island, NY 11794

Dr. J.W. Oldfield
Cortest Laboratories Ltd
23 Shepherd Street
Sheffield, S3 7BA, U.K.

Ms. D.M. Aylor
Code 613
Naval Surface Warfare Center
Annapolis, MD 21402-5067

Prof. K. Sieradzki
Dept. of Materials Sci. & Eng.
The Johns Hopkins University
Baltimore, MD 21218

Dr. P.S. Pao
Code 6326
Naval Research Laboratory
Washington, D.C. 20375-5343

Dr. W.P. Allen
United Technologies Research
Ctr.
East Hartford, CT 06108

Dr. B.A. Shaw
Dept. of Eng. Sci. & Mechanics
207 Hallowell Building
The Pennsylvania State University
University Park, PA 16802-1484

Dr. P. Cox
SRI International
333 Ravenswood Ave.
Menlo Park, CA 94025-3493

Dr. R. E. Ricker
National Institute of Standards
and Technology
Bldg. 223, Room B-266
Gaithersburg, MD 20899

Dr. F.B. Mansfeld
Dept. of Materials Science
University of Southern California
University Park
Los Angeles, CA 90089-0241

Prof. R.E. White
Dept. of Chemical Engineering
University of South Carolina
Columbia, SC 29208

Prof. R.A. Buchanan
Dept. of Materials Science & Eng.
University of Tennessee
Knoxville, TN 37996-2200

Dr. B.J. Little
NRL Detachment
Bldg. 1105, Room D415
Stennis Space Center
MS 39529-5004

Prof. M.E. Orazem
Dept. of Chemical Engineering
University of Florida
Gainesville, FL 32611

Prof. J. O'M. Bockris
Dept. of Chemistry
Texas A & M University
College Station, TX 77843

Dr. V. S. Agarwala
Code 6062
Naval Air Warfare Center
Warminster, PA 18974-0591

Prof. R.C. Newman
UMIST
Corrosion and Protection Center
P.O. Box 88
Manchester M60 1QD, U.K.

Prof. S. C. Dexter
College of Marine Studies
University of Delaware
700 Pilottown Rd
Lewes, DE 19958

Prof. R.P. Gangloff
Dept. of Mat'ls Science & Eng.
Thornton Hall
University of Virginia
Charlottesville, VA 22903-2442

Dr. R. Brown
Dept. of Chemical Engineering
University of Rhode Island
Kingston, R.I. 02881-0805

Dr. J. Jones-Meehan
Code R301
Naval Surface Warfare Center
10901 New Hampshire Ave.
Silver Spring, MD 20903

Dr. P. Natishan
Code 6322
Naval Research Laboratory
Washington, D.C. 20375-5343

Dr. R. L. Jones
Code 6170
Naval Research Lab.
Washington, D.C. 20375-5342